



Efficient Failure Probability Calculations and Modeling Interface Debonding in TRISO Particles with Bison

30 September 2021

Technical Report

Wen Jiang¹, Gyanender Singh¹, Jason D. Hales¹, Aysenur Toptan¹, Benjamin W. Spencer¹, and Stephen R. Novascone¹

¹Idaho National Laboratory



DISCLAIMER

This information was prepared as an account of work sponsored by an agency of the U.S. Government. Neither the U.S. Government nor any agency thereof, nor any of their employees, makes any warranty, expressed or implied, or assumes any legal liability or responsibility for the accuracy, completeness, or usefulness, of any information, apparatus, product, or process disclosed, or represents that its use would not infringe privately owned rights. References herein to any specific commercial product, process, or service by trade name, trade mark, manufacturer, or otherwise, does not necessarily constitute or imply its endorsement, recommendation, or favoring by the U.S. Government or any agency thereof. The views and opinions of authors expressed herein do not necessarily state or reflect those of the U.S. Government or any agency thereof.

Efficient Failure Probability Calculations and Modeling Interface Debonding in TRISO Particles with Bison

Technical Report

Wen Jiang¹, Gyanender Singh¹, Jason D. Hales¹, Aysenur Toptan¹, Benjamin W. Spencer¹, and
Stephen R. Novascone¹

¹Idaho National Laboratory

30 September 2021

**Idaho National Laboratory
Computational Mechanics and Materials Department
Idaho Falls, Idaho 83415**

<http://www.inl.gov>

**Prepared for the
U.S. Department of Energy
Office of Nuclear Energy
Under U.S. Department of Energy-Idaho Operations Office
Contract DE-AC07-05ID14517**

ABSTRACT

This document constitutes completion of the NEAMS milestone, which is titled: *Demonstrate efficiency improvements in TRISO failure probability calculations and the effect of debonding on fission product transport in TRISO fuel particles in Bison*. In this report we present the development of : (1) the anisotropic elasticity model of pyrolytic carbon and extended material models using the local coordinate system for aspherical particle geometry, (2) a capability of modeling interface debonding in TRISO particles , (3) an efficient high-fidelity approach to calculate the failure probability of TRISO particles. Benchmark problems and AGR-2 tests are used to verify the models and demonstrate these new capabilities.

ACKNOWLEDGMENT







The submitted manuscript was authored by a contractor of the U.S. Government under contract DE-AC07-05ID14517. Accordingly, the U.S. Government retains a non-exclusive, royalty-free license to publish or reproduce the published form of this contribution, or allow others to do so, for U.S. Government purposes.

This research made use of the resources of the High Performance Computing Center at INL, which is supported by the Office of Nuclear Energy of the U.S. Department of Energy and the Nuclear Science User Facilities under contract DE-AC07-05ID14517.

DECLARATION OF COMPETING INTEREST

The authors declare that they have no known competing financial interests or personal relationships that could have appeared to influence the work reported in this technical report.

ORCID

Wen Jiang		orcid.org/0000-0001-6978-9159
Gyanender Singh		orcid.org/0000-0003-1828-4438
Jason D. Hales		orcid.org/0000-0003-0836-0476
Aysenur Toptan		orcid.org/0000-0003-4250-6336
Benjamin W. Spencer		orcid.org/0000-0002-8774-4445
Stephen R. Novascone		orcid.org/0000-0002-3938-4326

CONTENTS

Abstract	iii
List of Figures	vi
List of Tables	vii
Acronyms	1
I Introduction	2
II TRISO Material Model Improvement	2
II-A Improvements	2
II-B Example Cases	3
II-B1 Incorporating anisotropy in the elasticity model of the PyC layer	3
II-B2 Overall improvements in the calculations	4
II-C Thermal Anisotropy	9
III Modeling Debonding in TRISO Fuel Particles	10
III-A Mesh Modifier for Creating Cohesive Zone Interfaces	10
III-B Bilinear Mixed-Mode Traction Separation Law	10
III-B1 Softening onset prediction	11
III-B2 Delamination propagation prediction	11
III-B3 Constitutive equation for mixed-mode loading	12
III-B4 Viscous regularization	12
III-C Thermal Heat Transfer between Debonded Layers	12
III-D TRISO Layer Debonding Examples	13
III-D1 Debonding of the IPyC from the SiC	13
III-D2 Debonding of the buffer from the IPyC	14
III-D3 Debonding of the buffer from the IPyC and IPyC cracking	20
III-D4 Debonding of the buffer, IPyC, and SiC layers	21
III-E Incorporate Debonding Failure into Monte Carlo Scheme	22
III-E1 Stress correlation for IPyC cracking	22
III-E2 Monte Carlo Scheme	23
IV Efficient High-fidelity TRISO Statistical Failure Analysis	28
IV-A Failure Modes	28
IV-A1 Pressure vessel failure	28
IV-A2 Irradiation-induced IPyC failure leading to SiC cracking	28
IV-A3 Pressure vessel failure of an aspherical particle	28
IV-B Weibull Failure Theory	28
IV-C Higher Order Stress Concentrations	30
IV-C1 Stress correlation for IPyC cracking	31
IV-C2 Stress correlation for an aspherical particle	31
IV-D Direct Integration Scheme	32
IV-D1 Integration of failure probability function	32
IV-D2 MOOSE Stochastic Tools module	33
IV-D3 Methodology	33
IV-E Benchmark Problems	35
IV-F AGR-2 Irradiation As-run Prediction	38
V Conclusion and Future Work	47
Bibliography	48

LIST OF FIGURES

1	Concept of local coordinate axes in a general layered-type geometry and a TRISO particle.	3
2	Variation of maximum radial stress with fluence in the IPyC, SiC, and OPyC layers of a spherical TRISO particle and an aspherical TRISO particle.	5
3	Variation of maximum tangential stress with fluence in the IPyC, SiC, and OPyC layers of a spherical TRISO particle and an aspherical TRISO particle.	6
4	Variation of failure probability with fluence in the IPyC and SiC layers of a spherical TRISO particle and an aspherical TRISO particle.	7
5	Variation of maximum radial and tangential stresses with fluence in the IPyC, SiC, and OPyC layers.	8
6	Variation of failure probability with fluence in the IPyC layer.	9
7	Three-block examples	10
8	Temperature contour plots with varying fill gas conductivity from the two-block verification example.	14
9	Temperature predictions across the center horizontal line from the two-block verification example.	15
10	Random scale factor for normal strength.	15
11	Damage evolution during debonding of the IPyC from the SiC	16
12	Radial stress in the IPyC, SiC, and OPyC layers during debonding of the IPyC from the SiC	16
13	Tangential stress in the SiC layer during debonding of the IPyC from the SiC	17
14	Time history of stress in the SiC layer during debonding of the IPyC from the SiC.	17
15	Damage evolution during debonding of the IPyC from the SiC in an aspherical particle	18
16	Damage evolution during debonding of the buffer from the IPyC with a bond strength of 80 MPa	18
17	Radial stress during debonding of the buffer from the IPyC with a bond strength of 80 MPa	19
18	Time history of stress in the IPyC layer during debonding of the buffer from the IPyC.	19
19	Partial debonding of the buffer from the IPyC layer.	20
20	Damage evolution during partial debonding of the buffer from the IPyC	20
21	Tangential stress during partial debonding of the buffer from the IPyC	21
22	Time history of stress in the IPyC layer during partial debonding of the buffer from the IPyC.	21
23	Damage evolution during debonding of the buffer from the IPyC and IPyC cracking	22
24	Tangential stress during debonding of the buffer from the IPyC and IPyC cracking	22
25	Time history of stress during debonding of the buffer from the IPyC and IPyC cracking.	23
26	Damage evolution during debonding of the buffer from the IPyC and the IPyC from the SiC layer	24
27	Radial stress during debonding of the buffer from the IPyC and the IPyC from the SiC layer	25
28	Time history of stress during debonding of the buffer, IPyC, and SiC layers.	26
29	Time histories of maximum tangential stress in the SiC layer for a 2-D model of a particle with debonding between the IPyC and SiC layers, as compared with a 1-D model of an intact particle.	26
30	MC scheme employed by Bison for calculating the failure probability of TRISO particles.	27
31	2-D axisymmetric model of postulated cracking of the IPyC layer, and comparison between applying and not applying pressure on crack surfaces.	29
32	2-D axisymmetric model of an aspherical particle, and time-dependent results for that model.	30
33	Example of stress correlation functions for IPyC cracking.	31
34	Example of stress correlation functions for an aspherical particle.	32
35	Integration values using MOOSE's sparse grid with different orders of the polynomials.	34
36	Quadrature point location.	34
37	Calculate the failure probability of TRISO particles in Bison: direct integration scheme using 1-D simulation with correlation functions.	35
38	Calculate the failure probability of TRISO particles in Bison: direct integration scheme using 2-D simulation.	36
39	UCO failure probability	38
40	UO ₂ failure probability	39
41	Linear regression results for UCO compacts: (a) temperature vs. probability of IPyC cracking, (b) fluence vs. probability of IPyC cracking, and (c) burnup vs. probability of IPyC cracking.	42
42	Linear regression results for UCO compacts: (a) temperature vs. probability of IPyC cracking, (b) fluence vs. probability of IPyC cracking, and (c) burnup vs. probability of overall SiC failure.	42
43	Inner-wall tangential stress histories in the SiC layer for AGR-2 Capsule 6 compacts.	43

44	Inner-wall tangential stress histories in the SiC layer for AGR-2 Capsule 5 compacts.	44
45	Inner-wall tangential stress histories in the SiC layer for AGR-2 Capsule 3 compacts.	45
46	Inner-wall tangential stress histories in the SiC layer for AGR-2 Capsule 2 compacts.	46

LIST OF TABLES

I	Simulation settings for the CZM properties.	13
II	Number of quadrature points for tensor grid.	33
III	Irradiation conditions for benchmark problems.	35
IV	Fuel parameters in benchmark problems.	36
V	Stress correlation factors and effective mean strength for benchmark problems.	37
VI	Quadratic stress correlation functions for benchmark problems.	37
VII	IPyC cracking probability for benchmark problems.	37
VIII	Failure probability for benchmark problems using Bison's direct integration scheme.	38
IX	UCO and UO ₂ parameters used in modeling the AGR-2 irradiation.	39
X	Compacts used in modeling the AGR-2 irradiation.	40
XI	Failure probability for AGR-2 compacts.	41

ACRONYMS

AGR	Advanced Gas Reactor
CZM	cohesive zone modeling
EFPD	effective full power days
IIDC	irradiation-induced dimensional changes
INL	Idaho National Laboratory
IPyC	inner pyrolytic carbon (PyC)
MC	Monte Carlo
MOOSE	Multiphysics Object-Oriented Simulation Environment
NASA	National Aeronautics and Space Administration
OPyC	outer PyC
PDF	probability density function
PIA	principle of independent action
POD	proper orthogonal decomposition
PVF	pressure vessel failure
PyC	pyrolytic carbon
SiC	silicon carbide
TRISO	tri-structural isotropic
1-D	one-dimensional
2-D	two-dimensional

I. INTRODUCTION

Over the last few years, the Bison fuel performance code [1] has undergone significant development to expand its tri-structural isotropic (TRISO) particle fuel performance modeling capabilities [2, 3, 4, 5, 6, 7, 8]. Such development included the implementation of material models from PARFUME [9] and the capability to perform statistical failure analysis on large sets of samples, utilizing a Monte Carlo (MC) scheme to execute fast-running, one-dimensional (1-D), spherically symmetric models. Some PARFUME material models are simplified to be isotropic and make 1-D assumptions that only work for perfectly spherical particles. Improvements are needed in these material models to enable accurate analysis of TRISO particles. Several potential failure mechanisms for TRISO fuel, including cracking of the inner PyC (IPyC) layer and pressure vessel failure of an aspherical particle, were considered in Bison failure analysis. Debonding is another important failure mechanism observed in recent Advanced Gas Reactor (AGR) experiments. For Bison, a capability must be developed for modeling debonding in TRISO and incorporating it into statistical failure analysis. One limitation of the MC scheme in predicting particle failure is that the number of necessary samples is very large to compute a relatively low failure probability, and the computational resources needed for the task are tremendous. Therefore, it is important that Bison be enhanced with a fast integration approach to greatly enhance the efficiency of failure probability calculations.

The recent development to improve TRISO failure analysis in Bison is summarized in this report, which begins with Section II describing improvements to material models to eliminate isotropic and 1-D spherical particle assumptions. Section III outlines the new capability to model interface debonding in TRISO particles by using Bison. Several debonding examples are considered for demonstration. The direct integration approach of calculating failure probability is described in Section IV. To demonstrate its improved efficiency, the new approach is used to compute the stress and failure probability of 48 AGR-2 compacts. Finally, a conclusion and discussion of future work are provided in Section V.

II. TRISO MATERIAL MODEL IMPROVEMENT

The original TRISO capability in Bison assumed isotropy for some of the material models; namely, elasticity and thermal models for PyC. Also, some other models (e.g., the models for irradiation-induced swelling and thermal expansion of PyC) assumed perfectly spherical geometry. These models were initially developed for PARFUME, based on 1-D assumptions. However, as reported in [9, 10], the PyC layer in a TRISO particle exhibits anisotropy, which can significantly alter the predicted mechanical and thermal behavior of a TRISO particle. Also, TRISO particles generally deviate from a perfect spherical geometry, and in many cases, the asphericity can be significant enough to invalidate the assumption of perfect spherical geometry. Thus, improvements were needed in these material models to enable accurate analysis of the TRISO particles.

A. Improvements

To incorporate anisotropy in a regular spherical or non-spherical TRISO model, the material properties along the radial and tangential directions must be defined. In finite element software, the material properties are defined along a particular direction, using a system of coordinate axes. A local coordinate axes system defines coordinate axes at every location in a finite element model. In Bison, the capability to define local coordinate axes at every location in a TRISO particle was developed. Using this local coordinate system, the material properties (e.g., the elastic modulus) and strains tensors could be defined and then transformed into the global coordinate system for finite element calculations. The details of this approach are described in the schematic shown in Figure 1.

Figure 1a shows a layer of material in which the local coordinate system is defined in such a way that one local coordinate axis is aligned along the layer, while another axis is aligned in the transverse direction to the layer. Using this coordinate system, anisotropic properties can be defined for this layer (e.g., an elastic modulus of 100 GPa along the layer, and 40 GPa in the direction perpendicular to the layer). Similarly, for the PyC layer in a TRISO particle, different properties can be defined along the radial and tangential directions, as shown in Figure 1b.

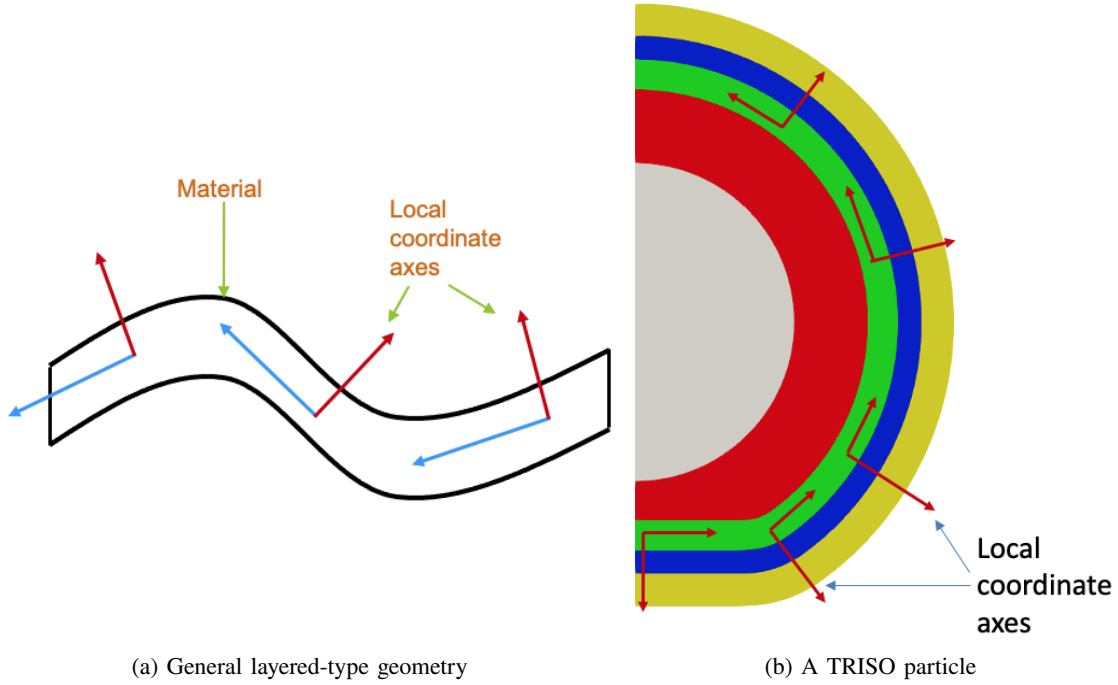


Fig. 1. Concept of local coordinate axes in a general layered-type geometry and a TRISO particle.

The local coordinate axes directions at a given quadrature point are determined using the normal vector at that point. The newly implemented algorithm in Bison (using `TRISO2DMeshGenerator`, `NormalVectorsTRISO`, and `TRISOGeometry`) determines the normal vector at any arbitrary point in the particle, irrespective of geometry type (i.e., spherical or aspherical). A transformation matrix is generated using these coordinate axes directions. The transformation matrix is then used to transform the elasticity tensor and the strain tensors from the local coordinate system into the global coordinate system (i.e., Cartesian coordinate system), or vice versa, as needed (`BisonUtils`). This capability was added to several TRISO material models, such as:

- The `PyCCEGAirradiationEigenstrain` material model that computes the irradiation-induced dimensional changes (IIDC) for PyC according to the CEGA
- The `PyCIrradiationEigenstrain` material model that computes the IIDC for PyC
- The `PyCThermalExpansionEigenstrain` material model that computes the thermal expansion (per K) and associated eigenstrain for PyC
- The `PyCCreepBase` base function that computes PyC creep
- The `PyCElasticityTensor` material model that computes the PyC elasticity tensor.

B. Example Cases

The benchmark problems described herein are used to demonstrate the improvements to the TRISO capability in Bison. These improvements are shown using the following two example cases: (1) incorporating anisotropy in the elasticity model of PyC (see Section II-B1), and (2) overall improvements in the calculations (see Section II-B2).

1) Incorporating anisotropy in the elasticity model of the PyC layer

The benchmark problem was solved using two types of PyC elasticity models: the isotropic elasticity model and the anisotropic elasticity model. These cases were analyzed for both the spherical and aspherical TRISO particle

geometries. The following equations show the elastic moduli in the radial and tangential directions for the case of anisotropic elasticity.

The radial and tangential components, E_r and E_t , of the elastic modulus E (GPa) are computed as [9, 10]:

$$E_r = 25.5 (0.384 + 0.324 \times 10^{-3} \rho) (1.463 - 0.463 BAF_0) \times (2.985 - 0.0662 L_c) (1 + 0.23 \phi) (1 + 0.00015 [T_C - 20]) \quad (1a)$$

$$E_t = 25.5 (0.384 + 0.324 \times 10^{-3} \rho) (0.481 + 0.519 BAF_0) \times (2.985 - 0.0662 L_c) (1 + 0.23 \phi) (1 + 0.00015 [T_C - 20]) \quad (1b)$$

where: ρ = the density (kg/m³)
 BAF_0 = the as-fabricated anisotropy (-)
 L_c = the crystallite diameter (30 angstroms)
 ϕ = the fast neutron fluence (10²⁵ n/m², $E > 0.18$ MeV)
 T_C = the temperature (°C).

For the isotropic elasticity model, the elastic modulus E is computed as:

$$E = \frac{E_r + 2E_t}{3} \quad (2)$$

The results comparing the maximum radial and tangential stresses and Weibull failure probabilities of the PyC and silicon carbide (SiC) layers for the spherical and aspherical particles are shown in Figures 2–4. The results indicate that the stresses and failure probabilities of the PyC and the SiC layers do not differ significantly for spherical particles.

However, for aspherical particles, the stresses and failure probabilities differ significantly. In general, the difference in the stress magnitudes is greatest at either around $1\text{--}2 \times 10^{25}$ n/m², when the stresses reach their peak value, or toward the end of the analysis. The Weibull failure probabilities for the PyC and SiC layers are greater at lower temperatures; the difference in the predicted failure probabilities for these two cases is also greater at lower temperatures. At a temperature of 973 K, the failure probability reaches one (i.e., the PyC layer fails quickly for both cases). These results indicate that the anisotropy in PyC elasticity is important for the aspherical TRISO particle, while for spherical particles, the predicted stresses and failure probabilities are similar to those obtained using the isotropic PyC elasticity model.

2) Overall improvements in the calculations

The benchmark problem was solved using the new TRISO material models, which account for anisotropy and provide the ability to analyze aspherical geometry, as well as using the old TRISO material models. The results comparing the stresses and Weibull failure probability in the PyC and SiC layers for these two cases are shown in Figures 5–6.

Figure 5 shows the maximum radial and tangential stresses in the inner PyC layer. The differences in the stress magnitudes obtained from the new and old TRISO models are significant. The difference is greatest at about $1\text{--}2 \times 10^{25}$ n/m² fluence, when the stresses reach their maximum magnitude, and toward the end of operation at about 5.6×10^{25} n/m². This difference in the stress magnitudes is significant at all the three temperatures considered in the analyses (973, 1273, and 1573 K). For both radial and tangential stresses, the maximum magnitude difference is about 30–40 MPa at the end of operation for an irradiation temperature of 1573 K.

Figure 5 shows the maximum radial and tangential stresses in the outer PyC layer. As for the inner PyC layer, the stress magnitude differences are significant at all three irradiation temperatures, and the maximum difference in the magnitude of stresses is about 30–40 MPa at the end of operation under the irradiation temperature of 1573 K. For the SiC layer, the variation of the maximum radial and tangential stresses with fluence is shown in Figure 5. The difference in the stress magnitudes for the SiC layer is lower (i.e., 10–20 MPa) than that for the PyC layers,

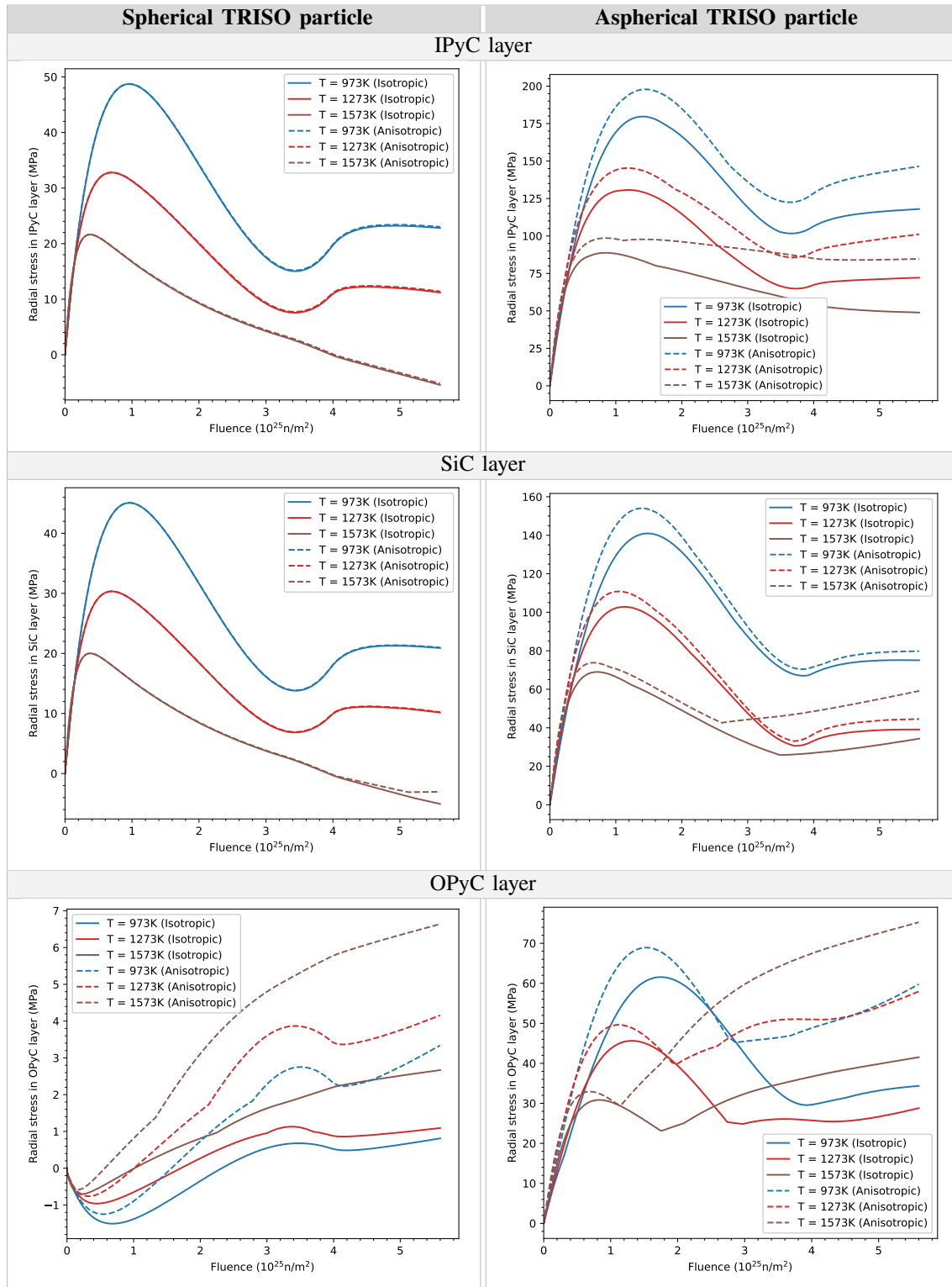


Fig. 2. Variation of maximum radial stress with fluence in the IPyC, SiC, and OPyC layers of a spherical TRISO particle (left column) and an aspherical TRISO particle (right column).

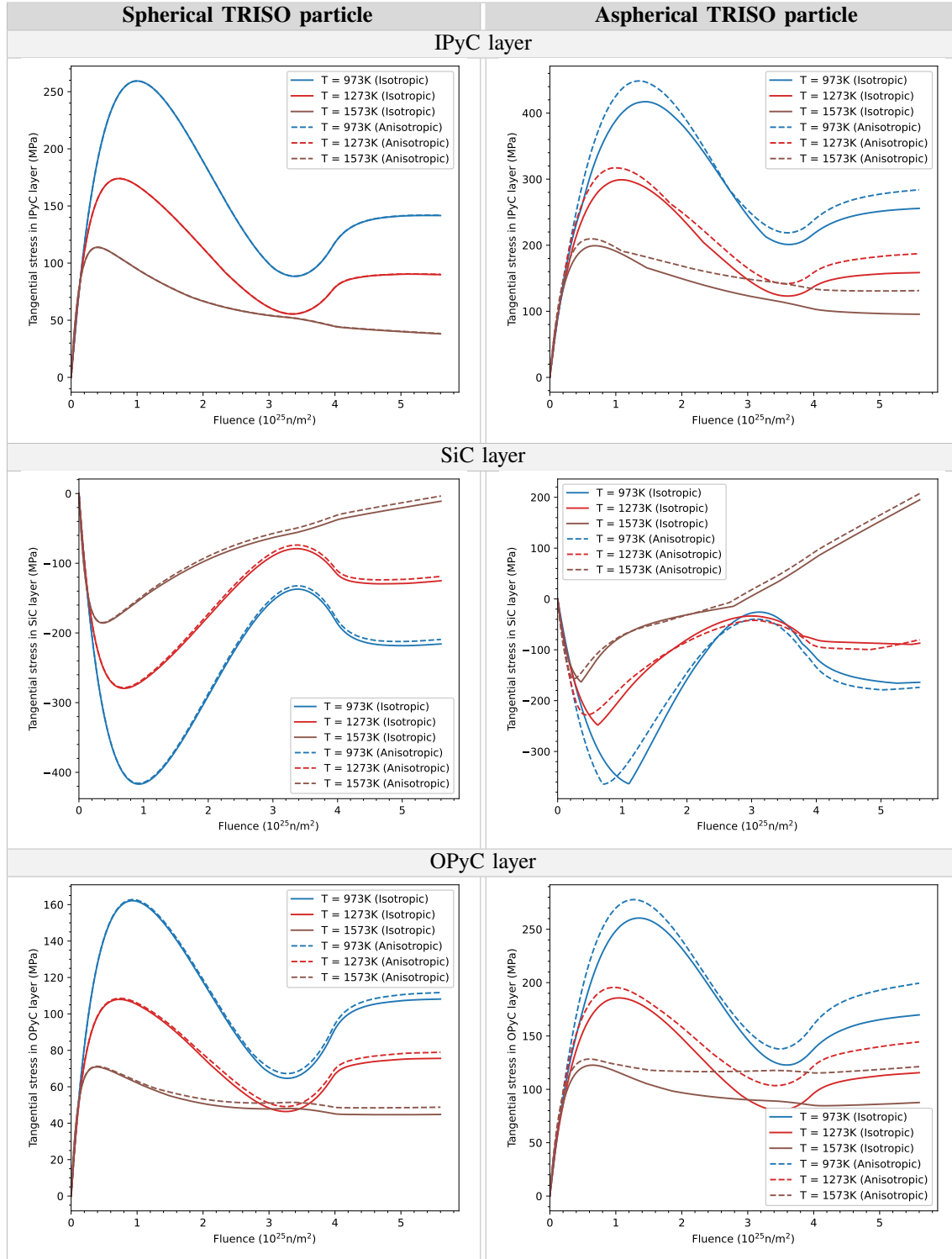


Fig. 3. Variation of maximum tangential stress with fluence in the IPyC, SiC, and OPyC layers of a spherical TRISO particle (left column) and an aspherical TRISO particle (right column).

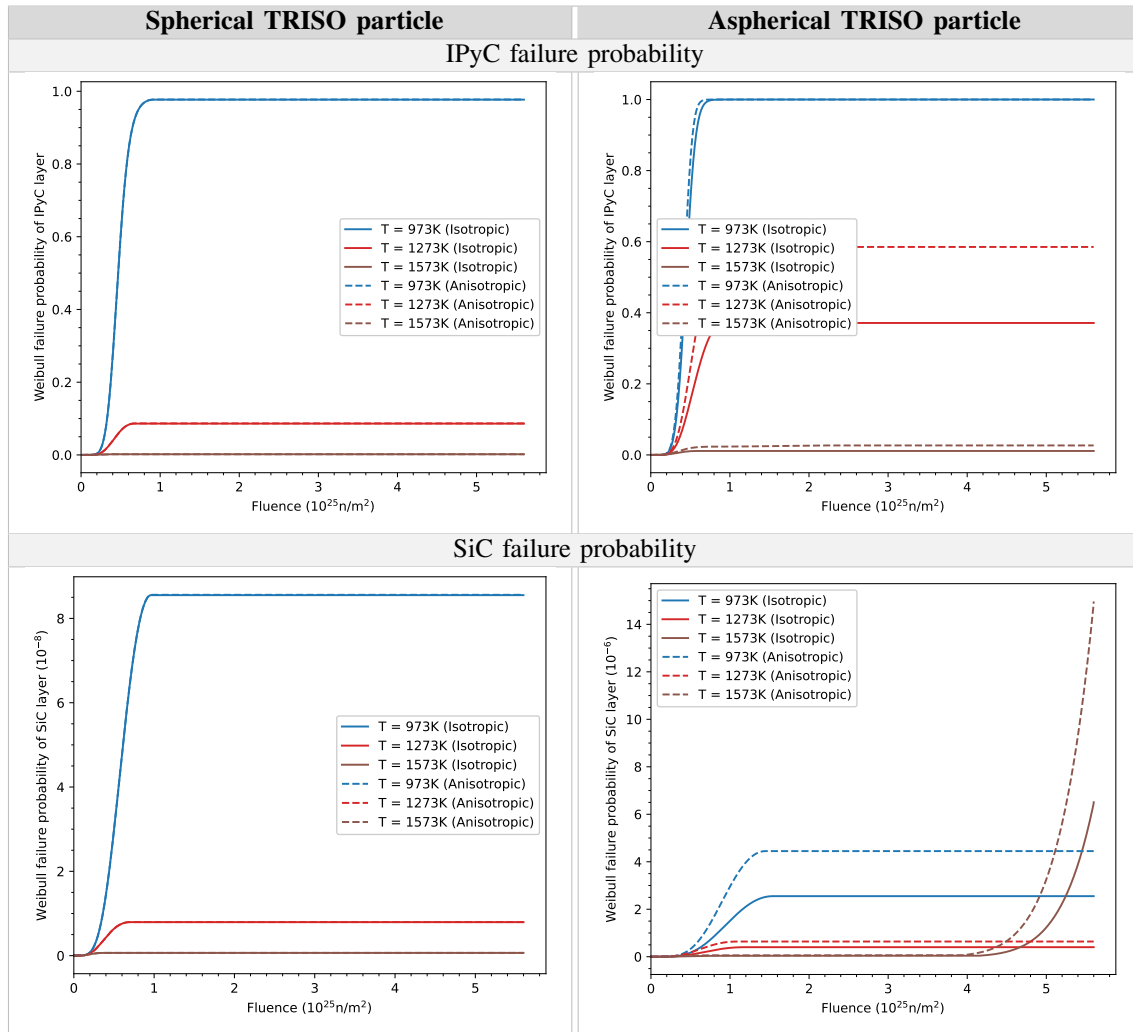


Fig. 4. Variation of failure probability with fluence in the IPyC and SiC layers of a spherical TRISO particle (left column) and an aspherical TRISO particle (right column).

except for the radial stress, for which the difference in the stress magnitude is greater than 30 MPa at the end of operation under a 1573 K irradiation temperature.

The calculated failure probability of the inner PyC layer using the new TRISO models is significantly higher than that calculated using old TRISO models at 1273 K, as shown in Figure 6. At the irradiation temperature of 1573 K, the failure probability is low and the difference between the two cases insignificant. However, at 973 K, the failure probability rises steeply to 1.0 for both cases, indicating that the PyC layer has cracked. The Weibull failure probability of the SiC layer is generally very low ($\approx 10^{-6}$). Since the new TRISO model predicts higher tensile stresses in the SiC layer at all the irradiation temperatures considered, the calculated failure probability is also higher. These results demonstrate that the new TRISO models significantly improve the predictions of TRISO behavior.

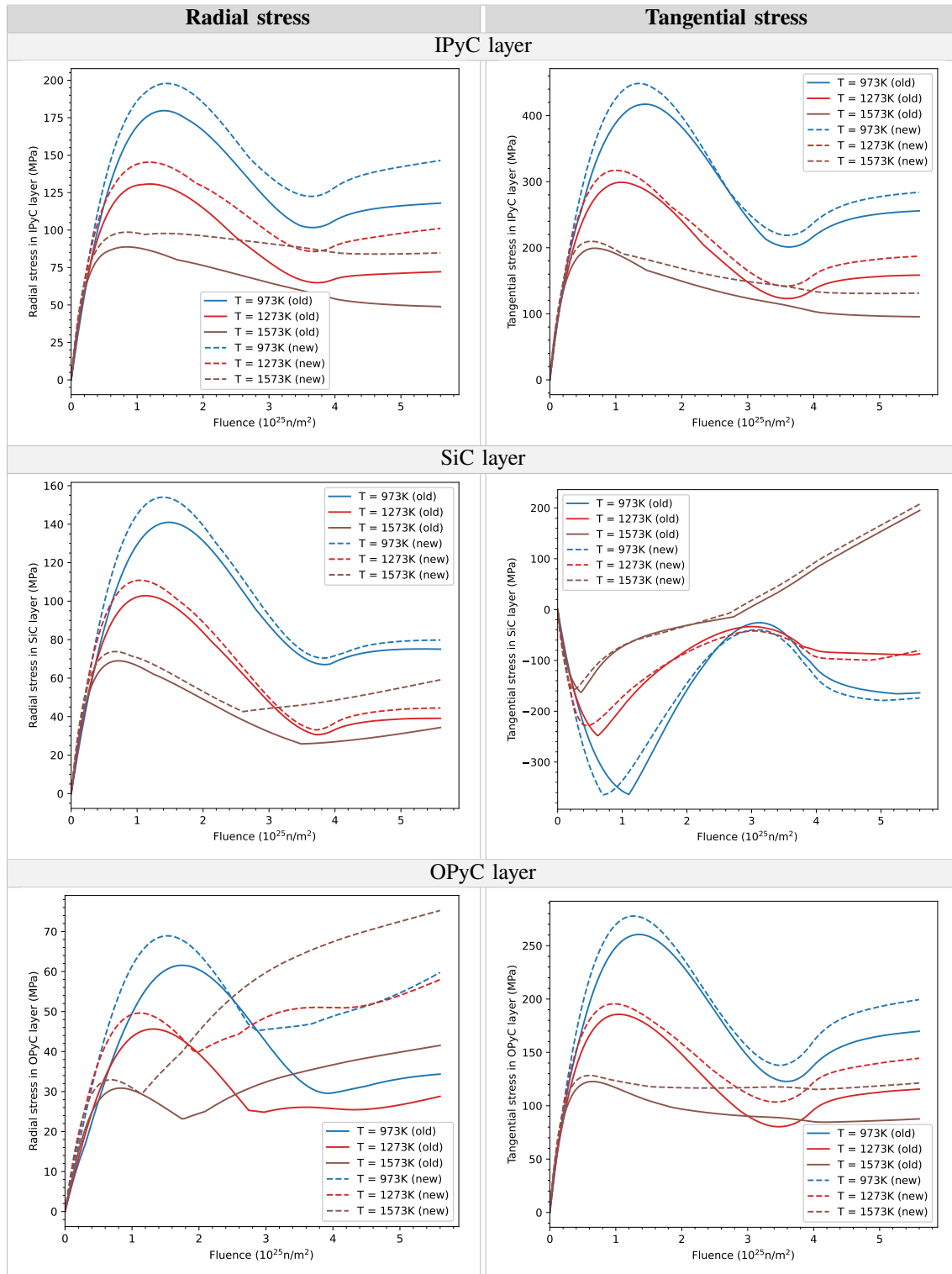


Fig. 5. Variation of maximum radial (left column) and tangential (right column) stresses with fluence in the IPyC, SiC, and OPyC layers.

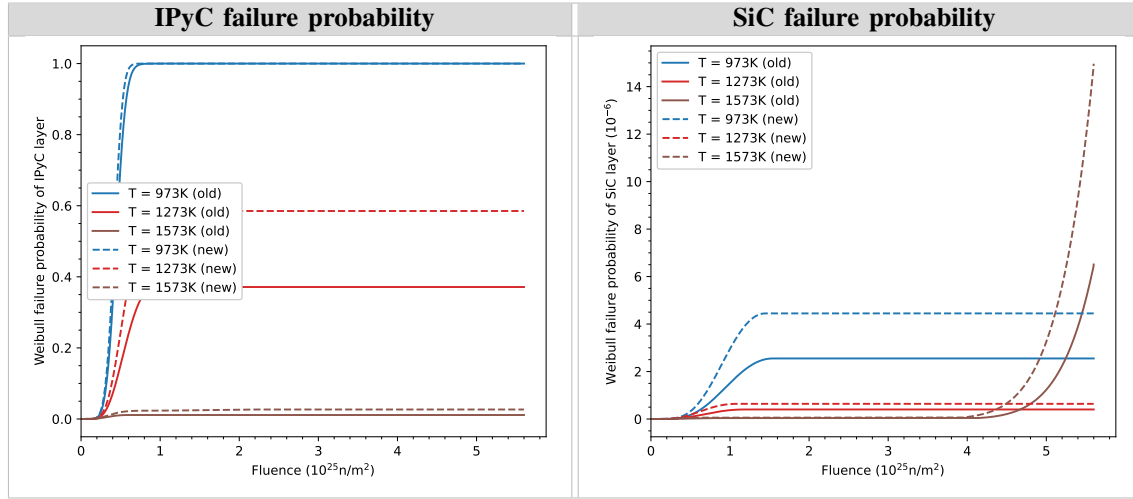


Fig. 6. Variation of failure probability with fluence in the IPyC layer.

C. Thermal Anisotropy

The PyC layer can exhibit anisotropy in its thermal properties. It has been reported that the thermal conductivity of PyC in the radial direction can be significantly lower than that in the tangential direction. This thermal anisotropy in the PyC layer can lead to very different thermal behavior of not only the PyC layer but also of the entire TRISO particle. To incorporate the thermal anisotropy, an anisotropic heat conduction kernel and a general purpose anisotropic heat conduction material that supports the transformation of the thermal conductivity tensor from one coordinate system to another was implemented in Multiphysics Object-Oriented Simulation Environment (MOOSE) (in the `AnisoHeatConduction` kernel and `AnisoHeatConductionMaterial` material model). Future work will involve developing an anisotropic PyC thermal model in Bison, based on these MOOSE models.

III. MODELING DEBONDING IN TRISO FUEL PARTICLES

Debonding of TRISO layers and the associated effects on the mechanical failure of TRISO particles is experimentally evident in recent AGR-1 [11] and AGR-2 [12] experiments. Buffers that are entirely debonded from the IPyC layer are typically observed in experiments, due to irradiation-induced shrinkage, and are not likely to cause cracking of the IPyC and SiC layers. Partial debonding at the buffer-IPyC interface results in stress concentrations in buffers, sometimes causing the IPyC layer to crack. Delamination at the IPyC-SiC interface was observed, potentially resulting in radial cracks in the SiC layer [13]. Debonding of the outer PyC (OPyC) may also occur during irradiation as the matrix shrinks away from the particles and pulls outward on the OPyC layer. Such experimental evidence highlights the importance of developing a capability in Bison to model TRISO layer interface debonding. Cohesive zone modeling (CZM) is a powerful tool for predicting delamination in adhesively bonded structures, and its framework was implemented in MOOSE [14]. This section summarizes new code development for the CZM and demonstrates several numerical examples of TRISO debonding.

A. Mesh Modifier for Creating Cohesive Zone Interfaces

A new type of block restricted option was added in MOOSE's `BreakMeshByBlockGenerator`. The new `block_pairs` option will only create interfaces between the specified block pairs. In addition, the `add_interface_on_two_sides` parameter enables interface boundaries to be generated on both sides of the interface, and these boundaries can be used to enforce thermal and mechanical contact at the interface.

An example of the mesh modifier is shown in Figure 7. The original mesh has three fully connected blocks. By using the `block_pairs = '2 3'` option, a CZM interface boundary between blocks 2 and 3 is created by appropriately duplicating nodes between the two blocks. With the `add_interface_on_two_sides = true` option, a second interface boundary is added on the other side of block 3. These two interface boundaries can be used as `primary` and `secondary` surfaces in MOOSE's thermal and mechanical constraints.

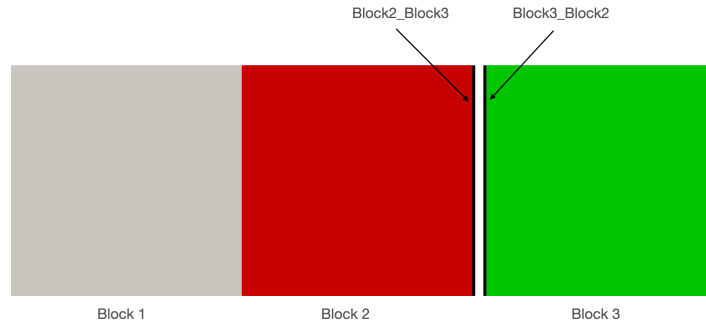


Fig. 7. Three-block example: two interface boundaries are created between block 2 and block 3, named “Block2_Block3” and “Block3_Block2”, respectively.

B. Bilinear Mixed-Mode Traction Separation Law

The bilinear mixed mode traction separation law described in [15] was implemented in MOOSE to model the initiation and propagation of debonding between TRISO layers. The model description is outlined below.

1) Softening onset prediction

Initiation of the softening process is predicted using the following quadratic failure criterion:

$$\left(\frac{\langle \tau_3 \rangle}{N}\right)^2 + \left(\frac{\tau_2}{S}\right)^2 + \left(\frac{\tau_1}{T}\right)^2 = 1 \quad (3)$$

where: N = interlaminar tensile strength
 S and T = interlaminar shear strengths
 τ_i = local traction

The Macaulay bracket $\langle \cdot \rangle$ is used to describe the ramp function:

$$\langle x \rangle = \begin{cases} 0, & x < 0 \\ x, & x \geq 0 \end{cases} \quad (4)$$

The total mixed-mode relative displacement δ_m is defined as:

$$\delta_m = \sqrt{\delta_1^2 + \delta_2^2 + \langle \delta_3 \rangle^2} = \sqrt{\delta_{shear}^2 + \langle \delta_3 \rangle^2} \quad (5)$$

where: δ_{shear} = the norm of the vector defining the tangential relative displacements of the element.

Using the same penalty stiffness in Modes I, II, and III, the tractions before softening onset are:

$$\tau_i = K \delta_i \quad (6)$$

for $i = 1, 2, 3$.

Assuming $S = T$, the single-mode relative displacements at the onset of softening are:

$$\delta_3^0 = \frac{N}{K} \quad (7)$$

and

$$\delta_1^0 = \delta_2^0 = \delta_{shear}^0 = \frac{S}{K} \quad (8)$$

For an opening displacement δ_3 greater than zero, the mode mixity ratio β is defined as:

$$\beta = \frac{\delta_{shear}}{\delta_3} \quad (9)$$

The mixed-mode relative displacement corresponding to the onset of softening δ_m^0 is given as:

$$\delta_m^0 = \begin{cases} \delta_3^0 \delta_1^0 \sqrt{\frac{1 + \beta^2}{(\delta_1^0)^2 + (\beta \delta_3^0)^2}} & \delta_3 > 0 \\ \delta_{shear}^0 & \delta_3 \leq 0 \end{cases} \quad (10)$$

2) Delamination propagation prediction

Two types of propagation criterion were implemented in MOOSE: (1) a power-law criterion, and (2) a Benzeggagh and Kenane (B-K) criterion. The mathematical formulations of each criterion are detailed below.

1) The power law criterion is given as:

$$\left(\frac{G_I}{G_{IC}}\right)^\alpha + \left(\frac{G_{II}}{G_{IIC}}\right)^\alpha = 1 \quad (11)$$

The mixed-mode displacements corresponding to total decohesion are given as:

$$\delta_m^f = \begin{cases} \frac{2(1+\beta^2)}{K\delta_m^0} \left[\left(\frac{1}{G_{IC}} \right)^\alpha + \left(\frac{\beta^2}{G_{IIC}} \right)^\alpha \right]^{-1/\alpha} & \delta_3 > 0 \\ \sqrt{(\delta_1^f)^2 + (\delta_2^f)^2} & \delta_3 \leq 0 \end{cases} \quad (12)$$

2) The B-K criterion, proposed by Benzeggagh and Kenane [16], is given as:

$$G_{IC} + (G_{IIC} - G_{IC}) \left(\frac{G_{shear}}{G_T} \right)^\eta = G_C \quad (13a)$$

with

$$G_T = G_I + G_{shear} \quad (13b)$$

The mixed-mode displacements corresponding to total decohesion are given as:

$$\delta_m^f = \begin{cases} \frac{2}{K\delta_m^0} \left\{ G_{IC} + \left(G_{IIC} - G_{IC} \left[\frac{\beta^2}{1+\beta^2} \right]^\eta \right) \right\} & \delta_3 > 0 \\ \sqrt{(\delta_1^f)^2 + (\delta_2^f)^2} & \delta_3 \leq 0 \end{cases} \quad (14)$$

3) *Constitutive equation for mixed-mode loading*

The constitutive equation for mixed-mode loading is given as:

$$\tau_s = D_{sr} \delta_r \quad (15a)$$

$$D_{sr} = \begin{cases} \bar{\delta}_{sr} K & \text{if } \delta_m^{max} \leq \delta_m^0 \\ \bar{\delta}_{sr} \left[(1-d)K + Kd\bar{\delta}_{s3} \frac{\langle -\delta_3 \rangle}{-\delta_3} \right] & \text{if } \delta_m^0 < \delta_m^{max} \leq \delta_m^f \\ \bar{\delta}_{s3}\bar{\delta}_{3r} \frac{\langle -\delta_3 \rangle}{-\delta_3} K & \text{if } \delta_m^{max} \geq \delta_m^f \end{cases} \quad (15b)$$

$$d = \frac{\delta_m^f (\delta_m^{max} - \delta_m^0)}{\delta_m^{max} (\delta_m^f - \delta_m^0)} \quad d \in [0, 1] \quad (15c)$$

4) *Viscous regularization*

Cohesive zone models that exhibit softening behavior and stiffness degradation often lead to convergence difficulties in an implicit solver. The traction separation laws can be regularized using viscosity. The viscous damage variable d_v is defined by:

$$\dot{d}_v = \frac{1}{\mu} (d - d_v) \quad (16)$$

where μ is the viscosity parameter representing the relaxation time of the viscous system. An analytical expression of d_v can be obtained using the backward Euler method. With viscous regularization, the d will be replaced by d_v in Equation 15b to compute traction.

C. Thermal Heat Transfer between Debonded Layers

Heat transfer across debonded layers is modeled using the following relation [17], neglecting the contribution of the solid contact conductance:

$$h_{gap} = h_g + h_r \quad (17a)$$

where: h_{gap} = the total conductance across the gap
 h_g = the gas conductance
 h_r = the conductance due to radiant heat transfer.

The fill gas conductance, h_g , is described as follows, assuming the continuum flow:

$$h_g = \frac{k_g}{d_g} \quad (17b)$$

where: k_g = the conductivity of the gas in the gap
 d_g = is the gap width.

The conductance due to radiant heat transfer, h_r , is computed as follows [18]:

$$h_r = \frac{\sigma(T_1^2 + T_2^2)(T_1 + T_2)}{1/\epsilon_1 + 1/\epsilon_2 - 1} \quad (17c)$$

where: σ = the Stefan–Boltzmann constant
 T_1, T_2 = the temperatures of the radiating surfaces
 ϵ_1, ϵ_2 = the emissivities of the surrounding radiating surfaces.

A two-block example was used to verify whether the thermal contact can be correctly enforced on the CZM interfaces. In this example, two interface boundaries were created by `BreakMeshByBlockGenerator`. The temperatures on the left and right boundary were set to 100 and 0 K, respectively. The two blocks were separated by a gap of 0.1 m. The thermal contact constraint was applied to transfer the heat from one block to the other. Four different gap conductivity values (i.e., 0.01, 0.1, 1, and 10 W/m-K) were considered. The temperature contours are shown in Figure 8. As the gap conductivity increases, more heat can be transferred from the left block to the right block. As shown in Figure 9, the temperature jump across the gap decreases as the gap conductivity increases. For a gap conductivity of 10 W/(m-K), the temperature is nearly continuous across the two blocks.

D. TRISO Layer Debonding Examples

In this section, the power-law propagation criterion was used as the criterion for delamination propagation. The CZM properties used in all the simulations are provided in Table I. For heat transfer across debonded layers, h_g was taken as 100 W/(m-K) and $\epsilon_1 = \epsilon_2 = 1$ (-). The fuel properties and simulation conditions are listed in Section IV-E. Condition 2—with an irradiation temperature of 973 K—was simulated for this report.

TABLE I. Simulation settings for the CZM properties.

G_{IC}	8 J/m ²	K	4×10 ¹⁴ N/m	S	10 MPa	μ	1 second
G_{IIC}	4 J/m ²	N	30 MPa	α	2		

To allow debonding to initiate at any arbitrary point, a scale factor with random values between 1.0 and 1.1 was applied to the normal strength, N. The random factor field is shown in Figure 10. The random factor values are generated for all elements but are used only at the interface where the CZM applies.

1) Debonding of the IPyC from the SiC

During irradiation, shrinkage of the IPyC layer induces a radial tensile stress at the interface between the IPyC and SiC layers. As shown in Figure 12, when the radial stress reaches a bond strength of 30 MPa, debonding of the IPyC from the SiC occurs. In this simulation, debonding initiates from the center, where the randomized normal strength is the weakest. During irradiation, it progressively propagates along the interface toward the two ends. It can be seen from Figure 13 that a stress concentration occurs in the SiC layer at the tip of the debonding region.

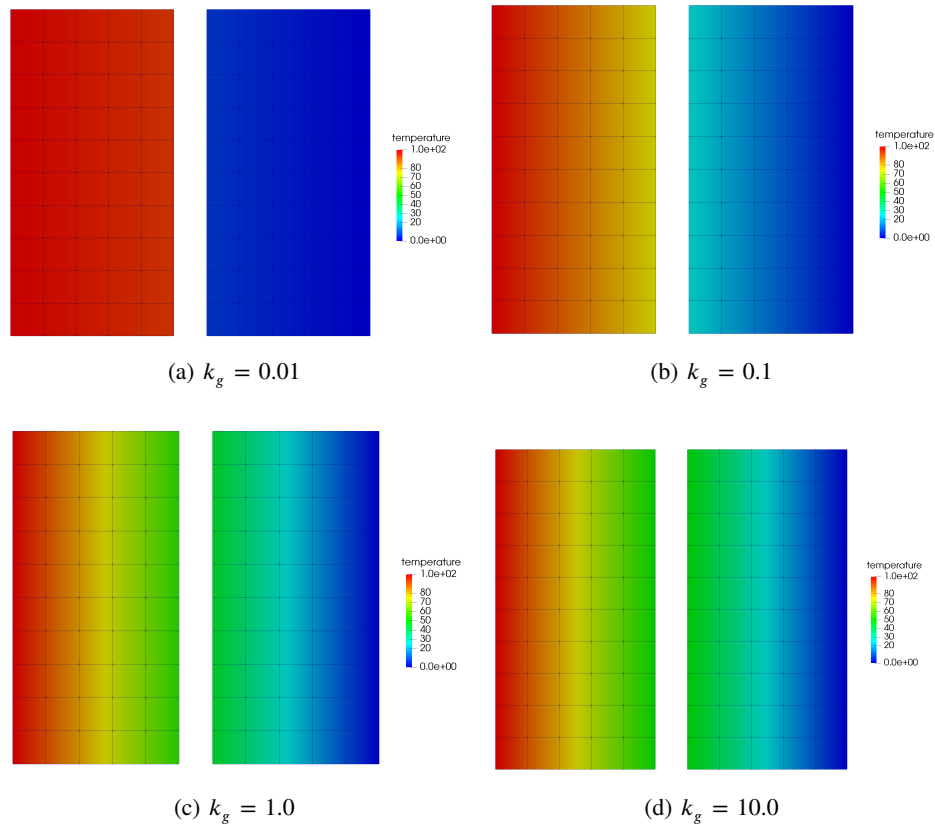


Fig. 8. Temperature contour plots with varying fill gas conductivity from the two-block verification example.

Although this stress is compressive under this simulation condition, it might become tensile and cause failure of the SiC layer when irradiation conditions change. The damage evolution is shown in Figure 11. At the end of irradiation, the interface is fully debonded at the bottom, yet remains connected at the top. The time history of stress in the SiC layer during debonding of the IPyC from the SiC is shown in Figure 14.

Next, debonding of the IPyC from the SiC layer was considered for an aspherical particle. A single flat facet created during fabrication on one side of the particle is a common cause of aspherical behavior in particle fuel. In Figure 15, it is interesting to see that the debonding initiates at the corner where a radial stress concentration occurs. This is different from the spherical particle case, in which the radial stress is uniform at the interface and the debonding initiates at the weakest strength point.

2) Debonding of the buffer from the IPyC

As the buffer layer shrinks under irradiation, a gap can form between the buffer and IPyC layer. Three cases were considered in this regard: (1) the buffer and IPyC are fully debonded at initial time, (2) debonding between the buffer and the IPyC with a bond strength of 30 MPa, and (3) debonding between the buffer and the IPyC with a bond strength of 80 MPa. The damage evolution and radial stress of debonding between the buffer and IPyC layers is shown in Figure 17 and Figure 20, respectively. In this simulation, the debonding initiates near the bottom of the interface and then propagates, fully separating the two layers. Due to the large shrinkage of the buffer layer, the radial stress is high, causing debonding to occur in the early irradiation stage. As seen from Figure 18, the radial stress reaches bond strength in a very early stage. The debonding produces a stress concentration in the tangential

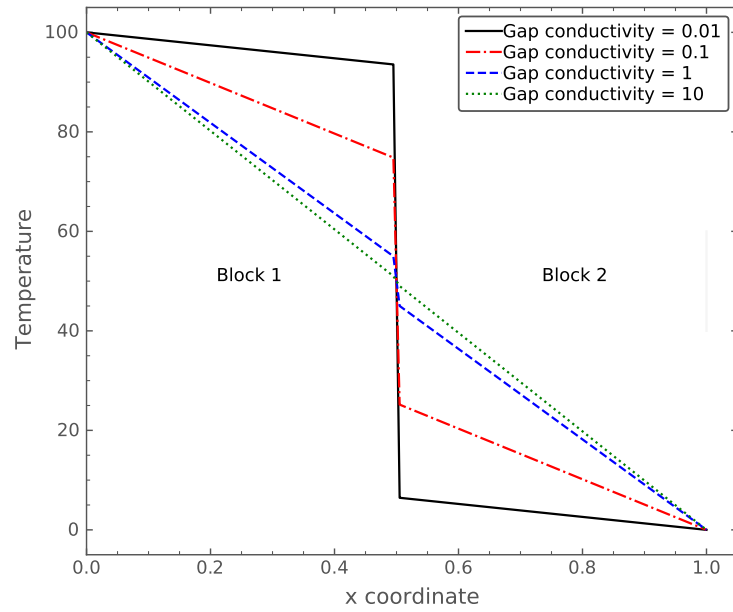


Fig. 9. Temperature predictions across the center horizontal line from the two-block verification example.

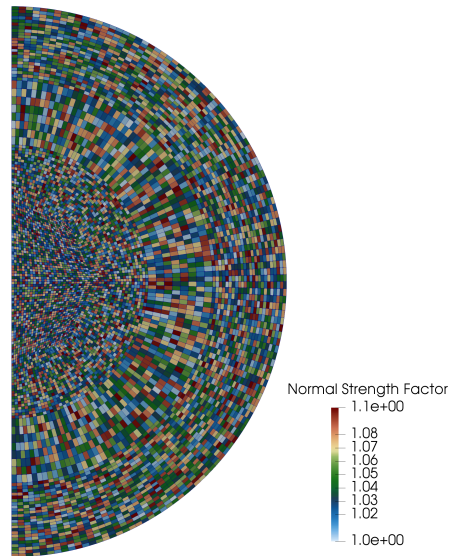


Fig. 10. Random scale factor for normal strength.

direction. After fully debonding, the stress remains the same as that in the case involving full initial debonding.

Fractures in irradiated IPyC layers were observed in AGR-1 experiments, suggesting that the IPyC layer could be torn during buffer–IPyC debonding at interfacial points where bonding was especially strong. The IPyC fractures were found immediately adjacent to the circumferential region that still had a bonded buffer–IPyC interface. An

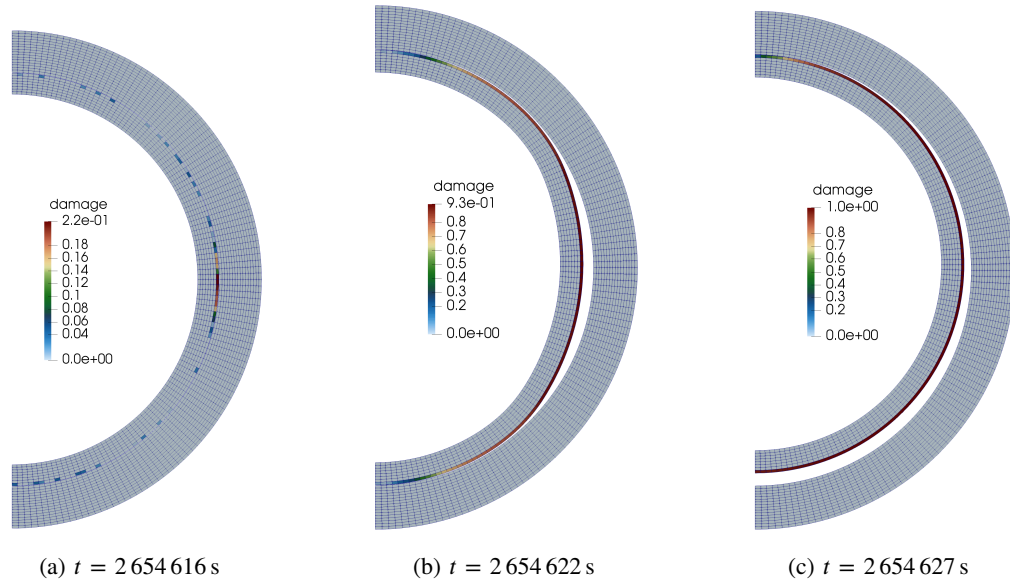


Fig. 11. Damage evolution during debonding of the IPyC from the SiC at $t =$ (a) 2 654 616 s, (b) 2 654 622 s, and (c) 2 654 627 s (displacements are magnified 10x).

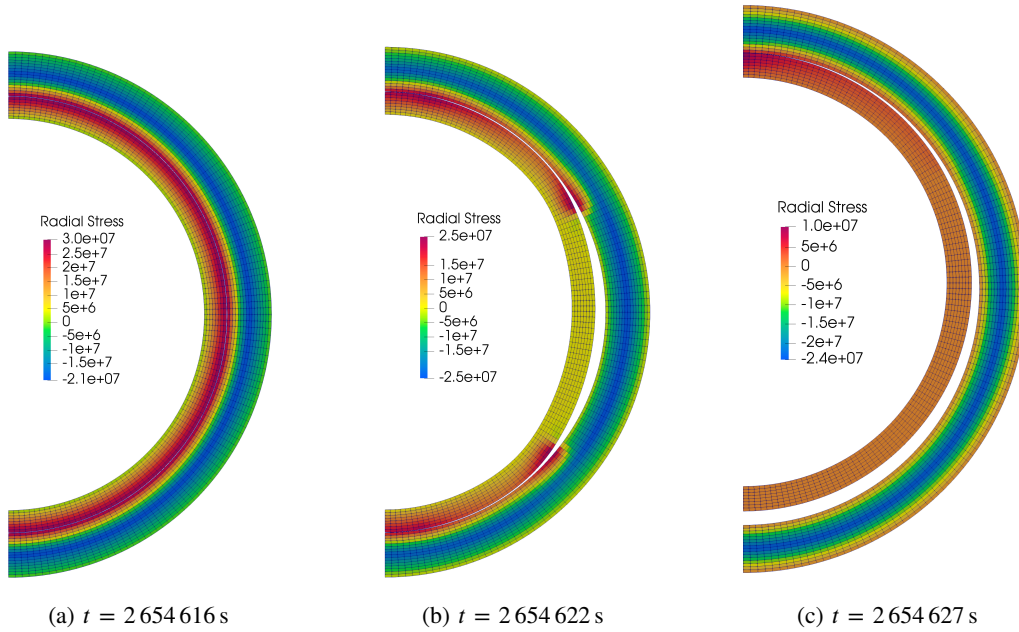


Fig. 12. Radial stress in the IPyC, SiC, and OPyC layers during debonding of the IPyC from the SiC at $t =$ (a) 2 654 616 s, (b) 2 654 622 s, and (c) 2 654 627 s (displacements are magnified 10x).

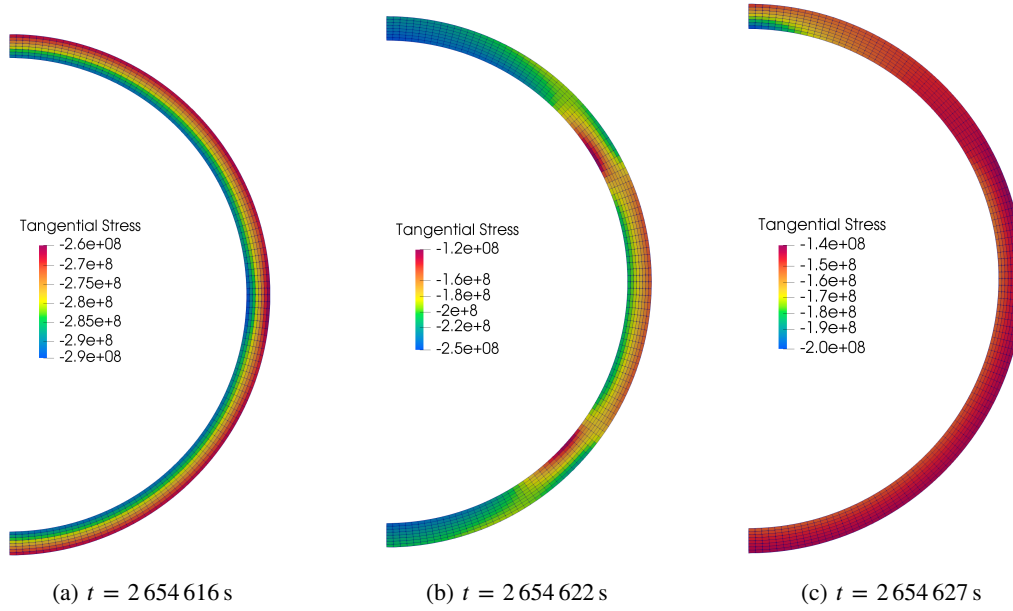


Fig. 13. Tangential stress in the SiC layer during debonding of the IPyC from the SiC at $t =$ (a) 2 654 616 s, (b) 2 654 622 s, and (c) 2 654 627 s.

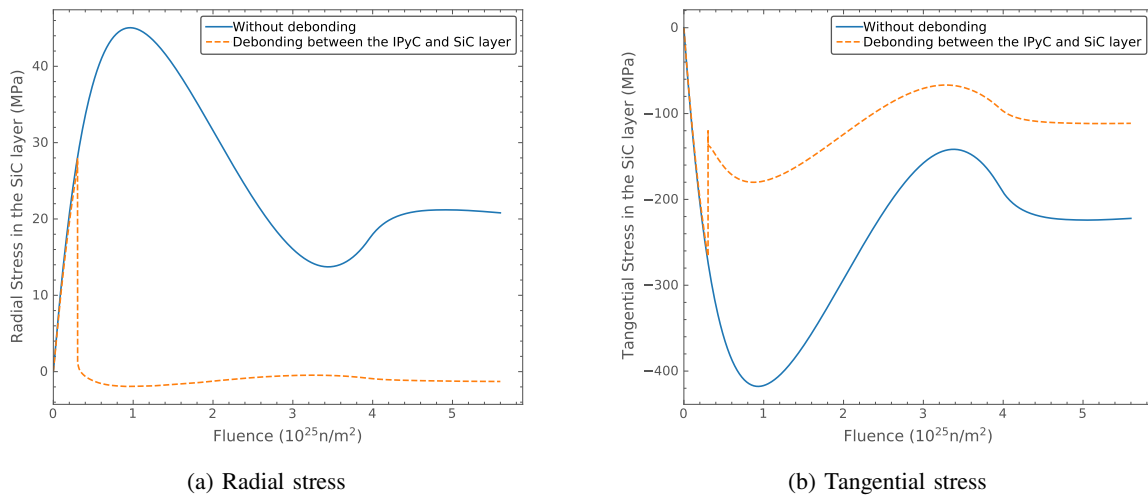


Fig. 14. Time history of stress in the SiC layer during debonding of the IPyC from the SiC.

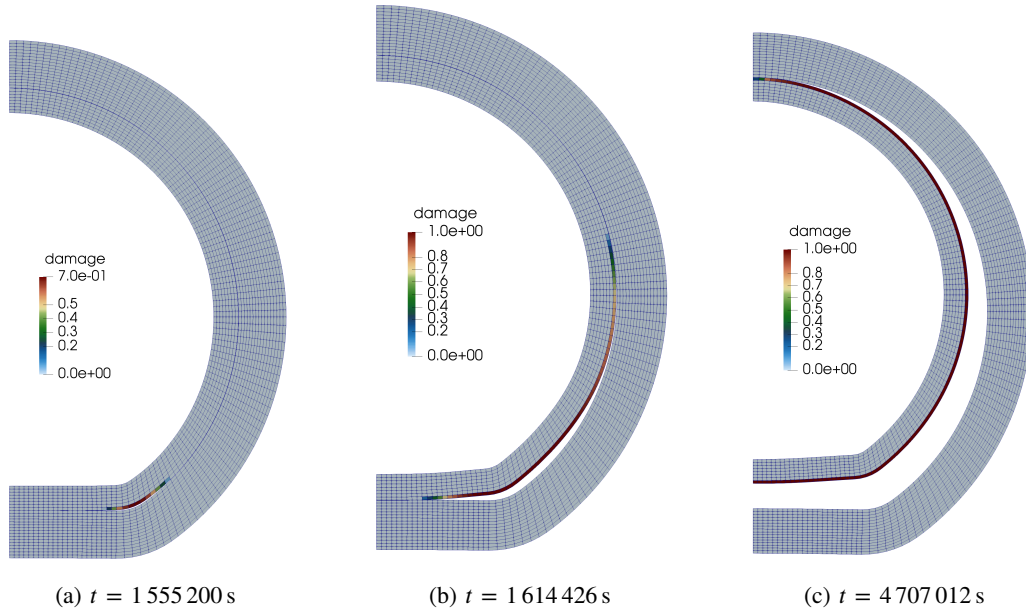


Fig. 15. Damage evolution during debonding of the IPyC from the SiC in an aspherical particle at $t =$ (a) 1 555 200 s, (b) 1 614 426 s, and (c) 4 707 012 s (displacements are magnified 10x).

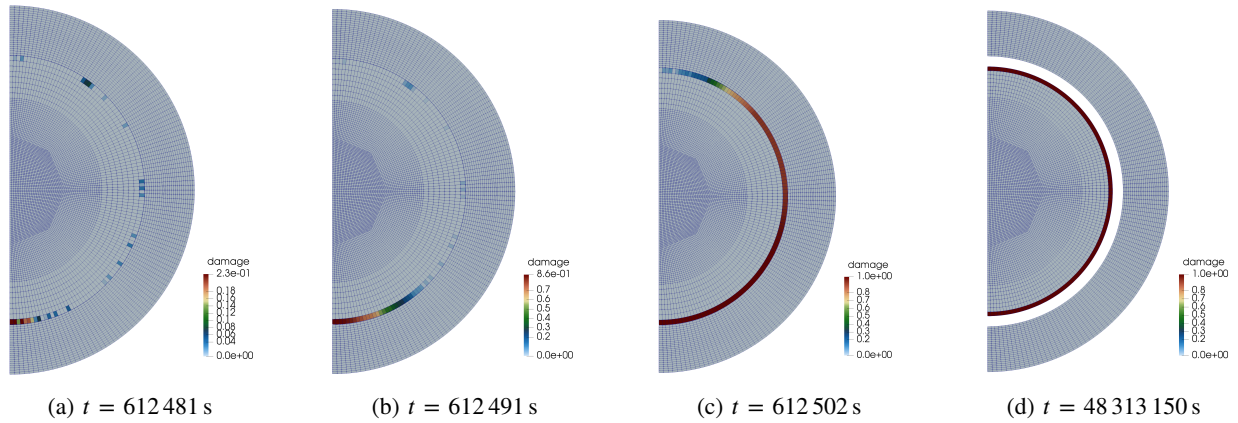


Fig. 16. Damage evolution during debonding of the buffer from the IPyC with a bond strength of 80 MPa at $t =$ (a) 612 481 s, (b) 612 491 s, (c) 612 502 s, and (d) 48 313 150 s.

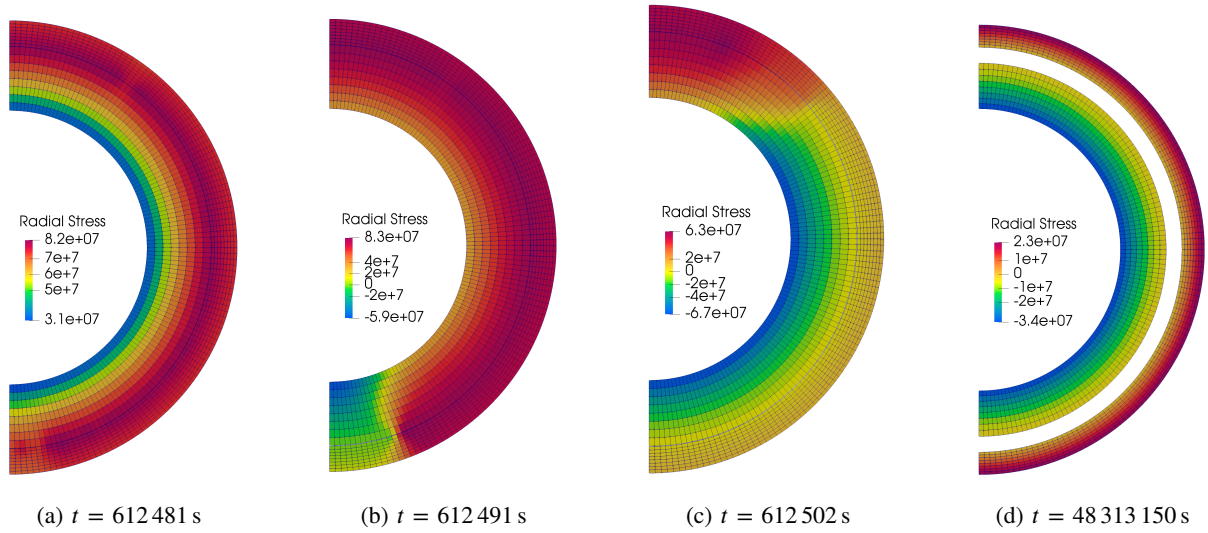


Fig. 17. Radial stress during debonding of the buffer from the IPyC with a bond strength of 80 MPa at $t =$ (a) 612481 s, (b) 612491 s, (c) 612502 s, and (d) 48313150 s.

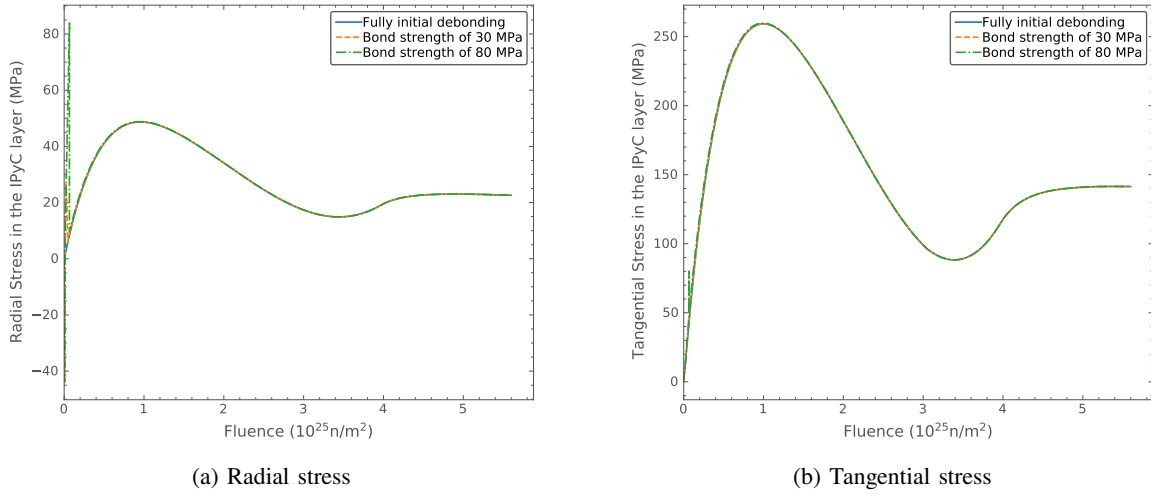


Fig. 18. Time history of stress in the IPyC layer during debonding of the buffer from the IPyC.

example was considered here to elucidate the effect of partial debonding on the IPyC fracture. As shown in Figure 19, the CZM interface was applied to only part of the buffer-IPyC interface, while keeping the top part fully connected. The damage evolution and radial stress of partial debonding between the buffer and IPyC layers is shown in Figure 20 and Figure 21, respectively. A stress concentration occurs at the debonded tip. The radial and tangential stresses in the IPyC layer are significantly higher than those produced by the fully debonded buffer and IPyC layers, and could potentially result in cracking of the IPyC layer. This is in good agreement with the experimental observation.

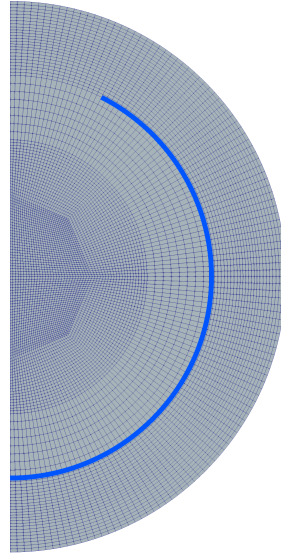


Fig. 19. Partial debonding of the buffer from the IPyC layer. The CZM interface is indicated in blue.

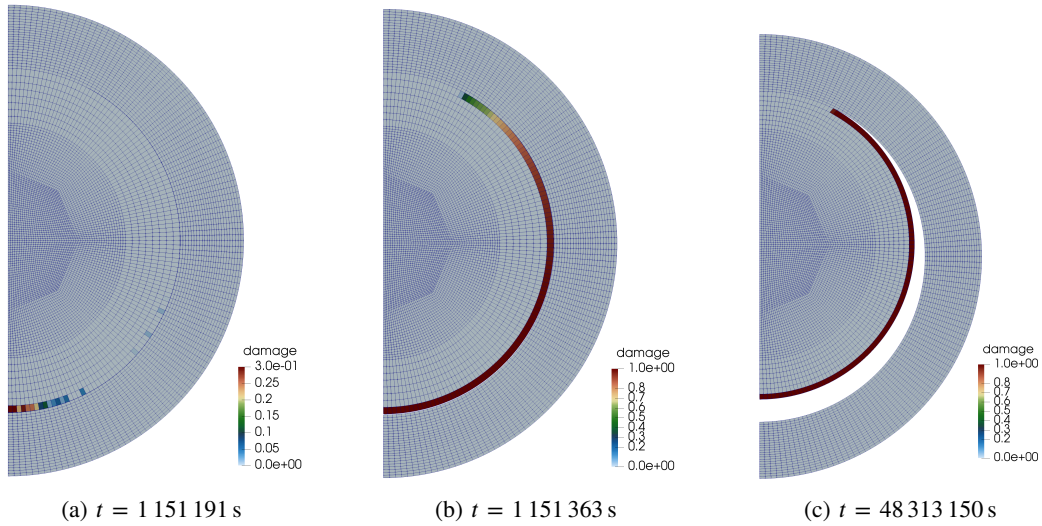


Fig. 20. Damage evolution during partial debonding of the buffer from the IPyC at $t =$ (a) 1 151 191 s, (b) 1 151 363 s, and (c) 48 313 150 s.

3) Debonding of the buffer from the IPyC and IPyC cracking

In addition to the debonding of the buffer from the IPyC layer, the cracking of the IPyC layer was also simulated using the CZM. The normal strength of the IPyC cracking was set at 80 MPa. From Figure 23 and Figure 24, cracking occurs after the buffer and IPyC were fully debonded. Such a crack leads to high local tensile stress in the SiC layer adjacent to the cracked IPyC, potentially causing failure of the SiC layer. The time history of stress in the IPyC and SiC layers is shown in Figure 25. The debonding does not have a large impact on the stress in the

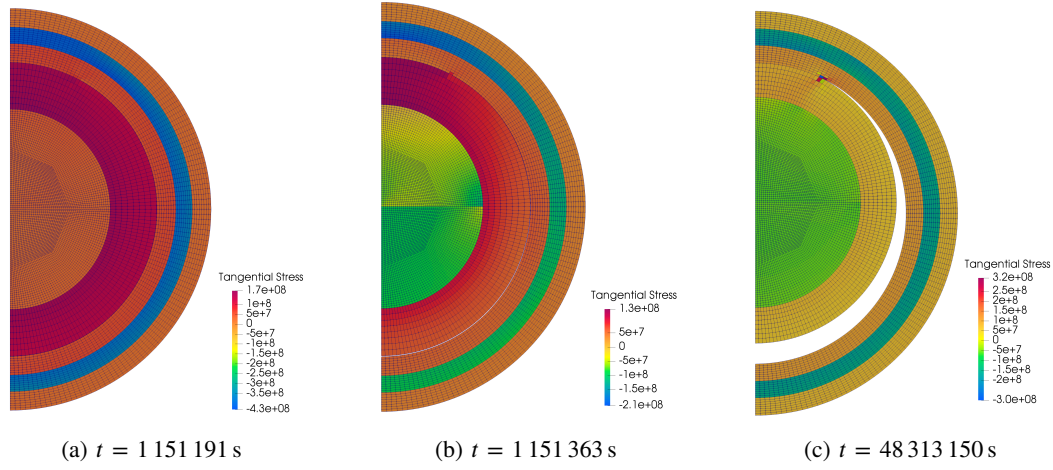


Fig. 21. Tangential stress during partial debonding of the buffer from the IPyC at $t =$ (a) 1 151 191 s, (b) 1 151 363 s, and (c) 48 313 150 s.

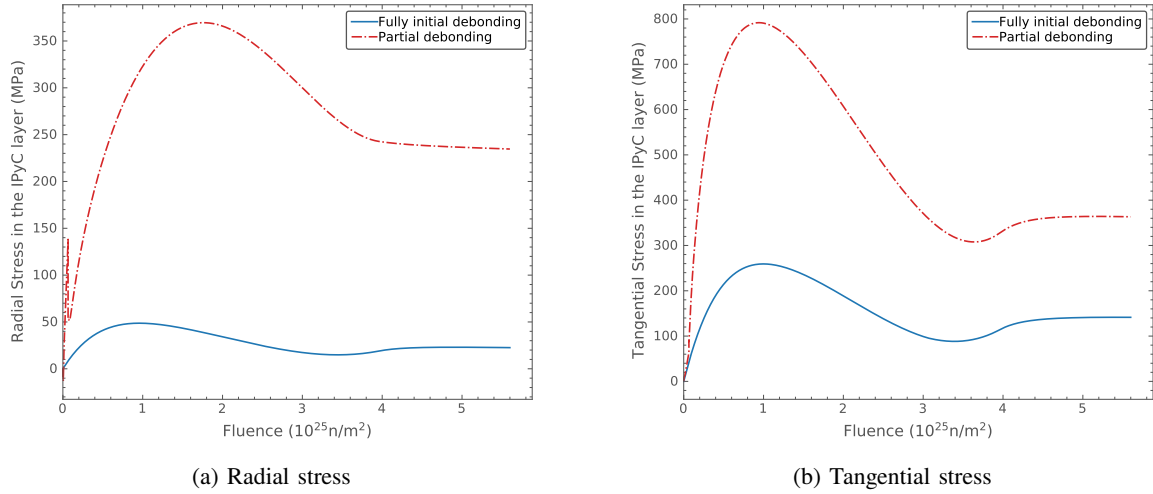


Fig. 22. Time history of stress in the IPyC layer during partial debonding of the buffer from the IPyC.

IPyC layer, whereas the cracking causes the SiC stress to change from compressive to tensile.

4) Debonding of the buffer, IPyC, and SiC layers

In the last example, debonding of both the buffer from the IPyC layer and the IPyC from the SiC layer was simulated. The damage evolution and radial stress is shown in Figure 26 and Figure 27, respectively. Although the bond strength of the buffer-IPyC and IPyC-SiC layers is the same, debonding of the buffer from the IPyC occurs first, because the radial stress between the buffer and IPyC layers reaches the critical bond strength sooner. The time history of tangential stress in the IPyC and SiC layers is shown in Figure 28.

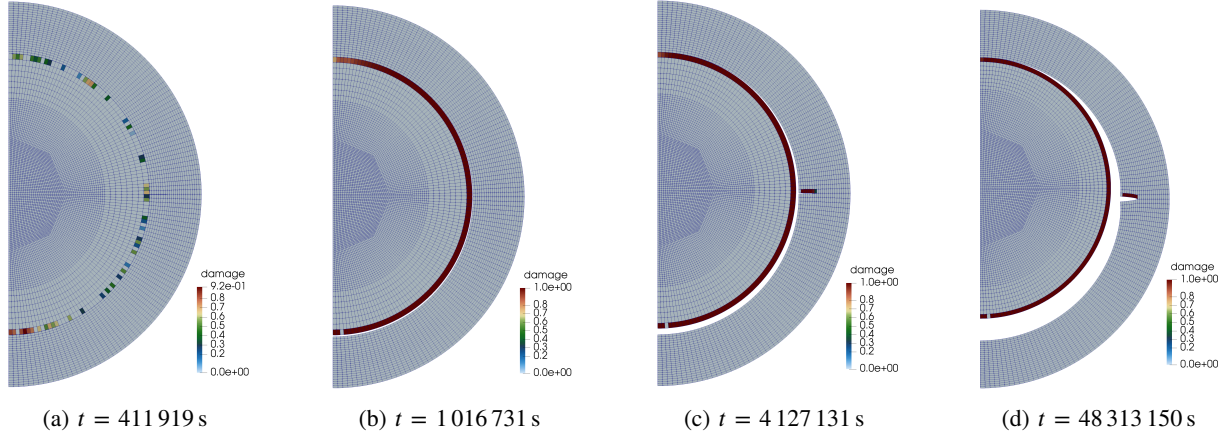


Fig. 23. Damage evolution during debonding of the buffer from the IPyC and IPyC cracking at $t =$ (a) 411 919 s, (b) 1 016 731 s, (c) 4 127 131 s, and (d) 48 313 150 s.

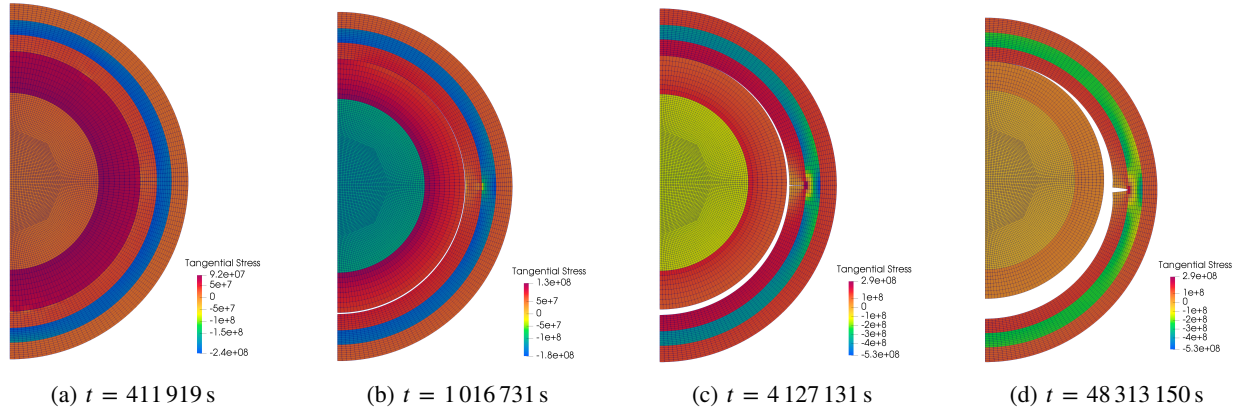


Fig. 24. Tangential stress during debonding of the buffer from the IPyC and IPyC cracking at $t =$ (a) 411 919 s, (b) 1 016 731 s, (c) 4 127 131 s, and (d) 48 313 150 s.

E. Incorporate Debonding Failure into Monte Carlo Scheme

1) Stress correlation for IPyC cracking

The maximum tangential stress histories in the SiC layer for both a debonded and an intact particle are shown in Figure 29. The maximum SiC stress in a debonded particle is approximated as:

$$\sigma_{\text{IPyC-SiC-debonding}} = \frac{\bar{\sigma}_{2D}}{\bar{\sigma}_{1D}} \sigma_{1D} \quad (18)$$

where $\bar{\sigma}_{2D}$ and $\bar{\sigma}_{1D}$ are the maximum stress calculated in the two-dimensional (2-D) and 1-D analyses, respectively, at the mean values for a specified batch of particles. Upon varying statistical parameters, the maximum stress in the SiC layer is determined from the 1-D finite element solution for σ_{1D} . The mean strength of the 2-D model, as evaluated at the maximum tangential stress state, will be used for 1-D analysis.

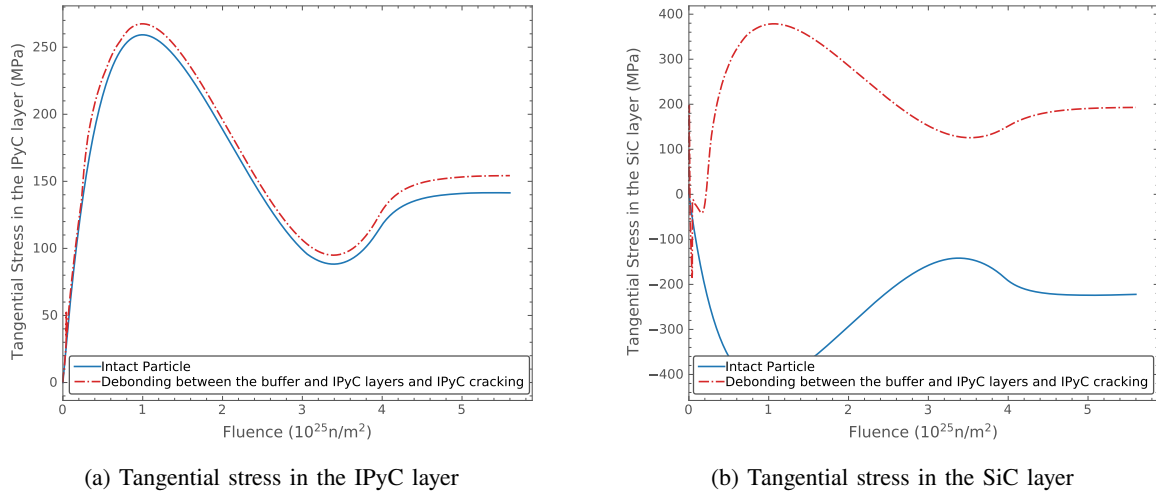


Fig. 25. Time history of stress during debonding of the buffer from the IPyC and IPyC cracking.

2) Monte Carlo Scheme

Figure 30 depicts the methodology used to calculate the failure probability of a population of TRISO particles. This methodology relies on an MC scheme in which each particle analyzed is a realization of a set of statistically sampled parameters from the distributions of as-fabricated fuel characteristics (e.g., dimensions and densities) that can be found among the particles in a fuel element. For each sample, Bison runs a 1-D model of a TRISO particle over the irradiation history. For particles with localized flaws (i.e., aspherical particles, particles with cracked IPyC, and particles with debonded IPyC and SiC), an adjustment of the maximum stress and effective mean strength will be made, as described in [4].

At each time step, the following failure mechanisms are checked:

- Pressure vessel failure of a spherical or aspherical particle: Failure occurs when the maximum tangential tensile stress in the SiC layer due to internal gas pressure exceeds the strength of the SiC.
- SiC failure due to IPyC cracking: Cracking of the IPyC occurs when the maximum tangential tensile stress in the IPyC layer exceeds its strength. A cracked IPyC changes stress from compressive to tensile in the SiC layer. SiC failure occurs when the maximum tangential tensile stress of the SiC layer due to IPyC cracking exceeds its strength.
- SiC failure due to debonding between the IPyC and SiC layers: Debonding of the IPyC and SiC layers occurs when the maximum radial stress at the interface exceeds its bond strength. A stress concentration in the SiC layer occurs at the tip of the debonded region. SiC failure occurs when the maximum tangential tensile stress in the SiC layer exceeds its strength, due to debonding".

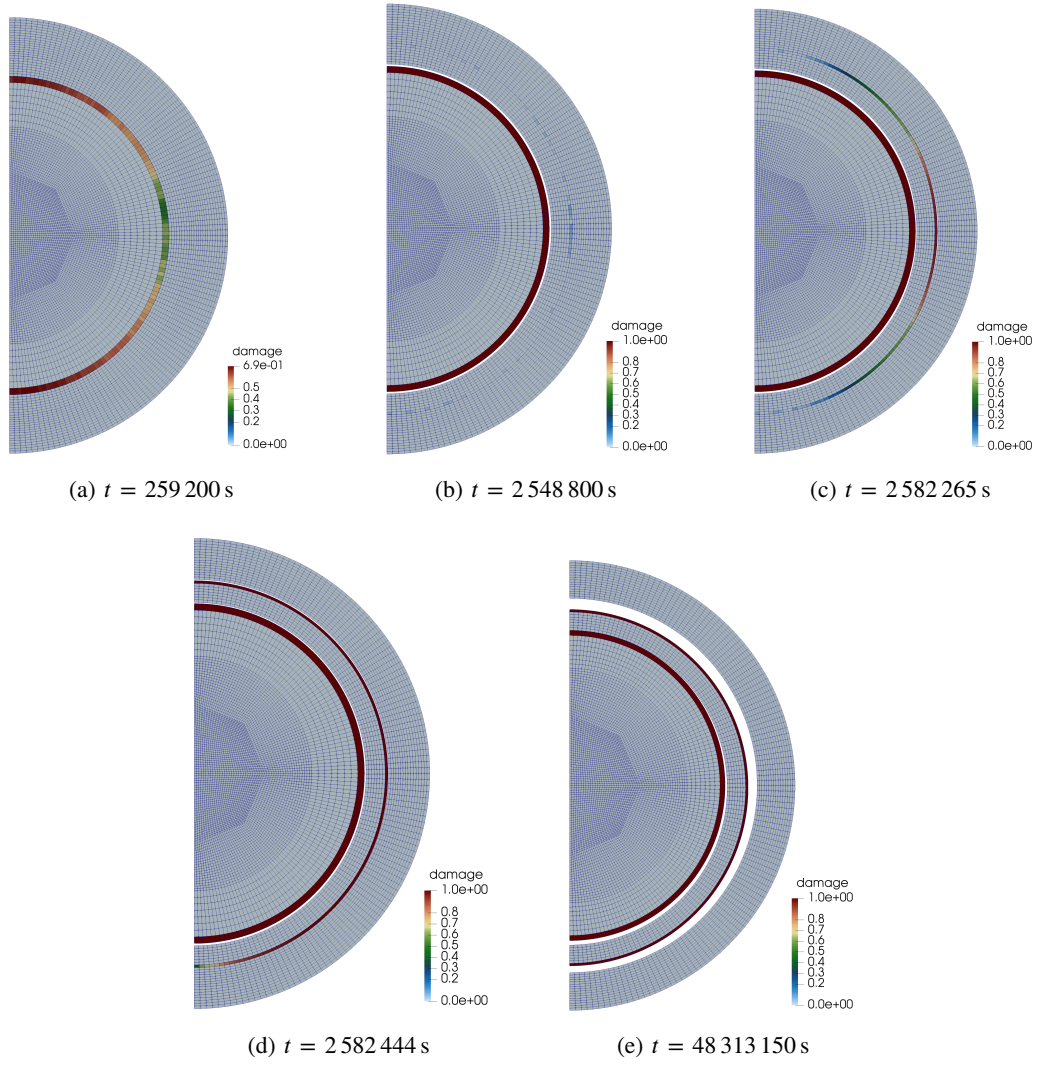


Fig. 26. Damage evolution during debonding of the buffer from the IPyC and the IPyC from the SiC layer at $t =$ (a) 259 200 s, (b) 2 548 800 s, (c) 2 582 265 s, (d) 2 582 444 s, and (e) 48 313 150 s.

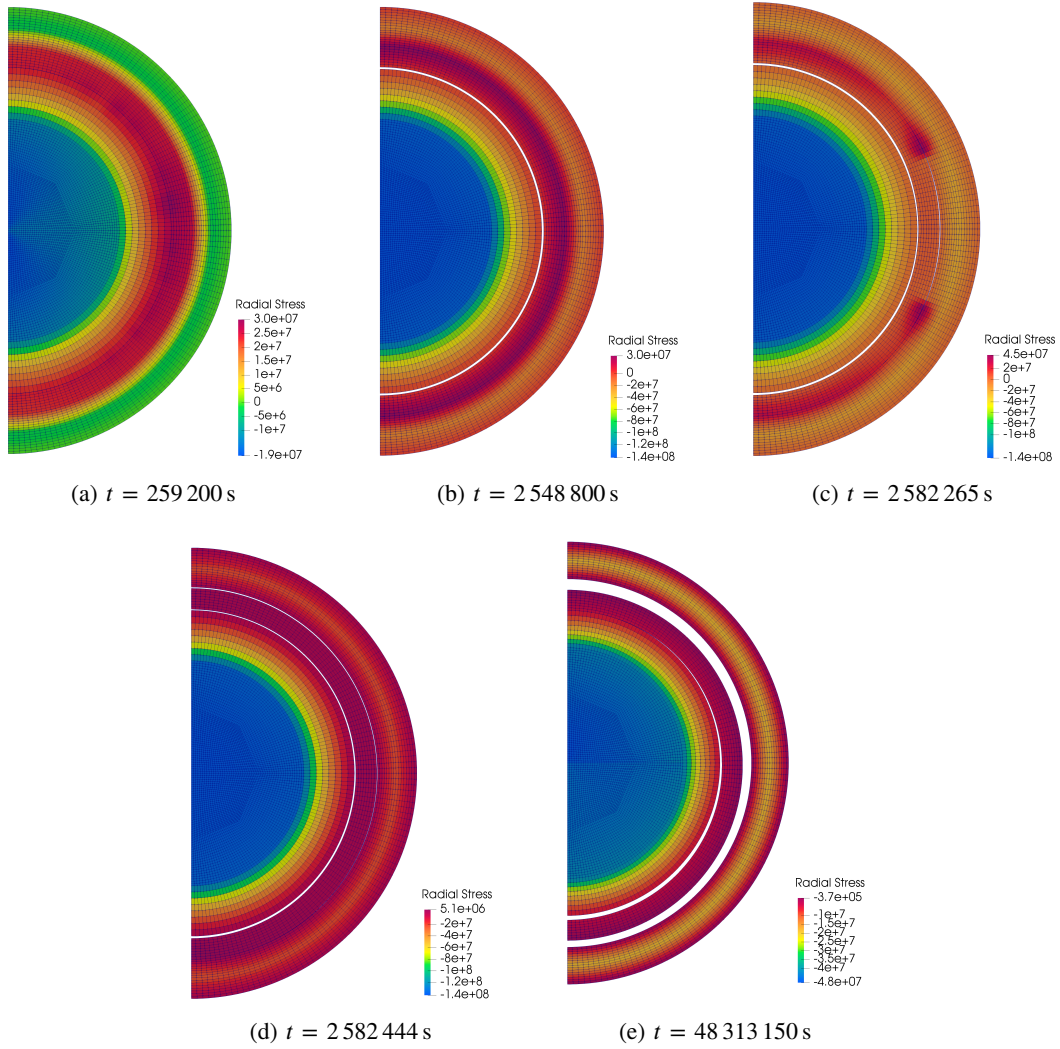
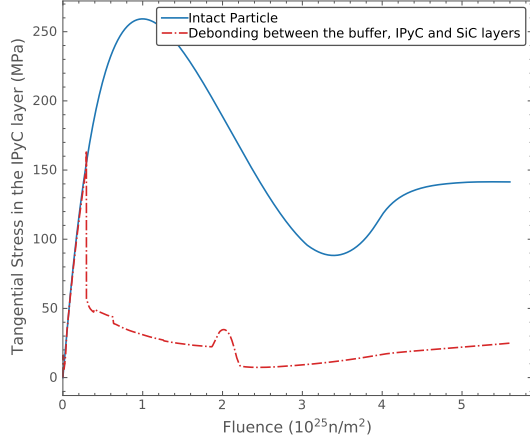
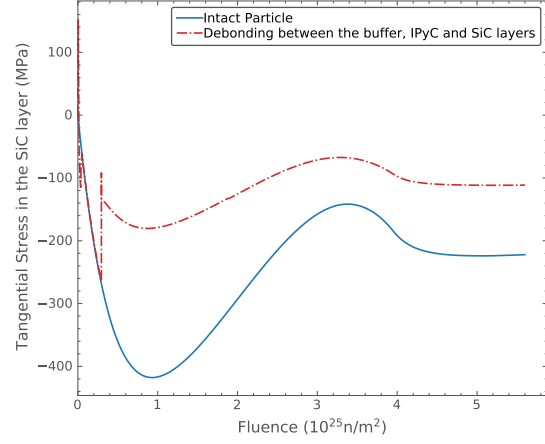


Fig. 27. Radial stress during debonding of the buffer from the IPyC and the IPyC from the SiC layer at $t =$ (a) 259 200 s, (b) 2 548 800 s, (c) 2 582 265 s, (d) 2 582 444 s, and (e) 48 313 150 s.



(a) Tangential stress in the IPyC layer



(b) Tangential stress in the SiC layer

Fig. 28. Time history of stress during debonding of the buffer, IPyC, and SiC layers.

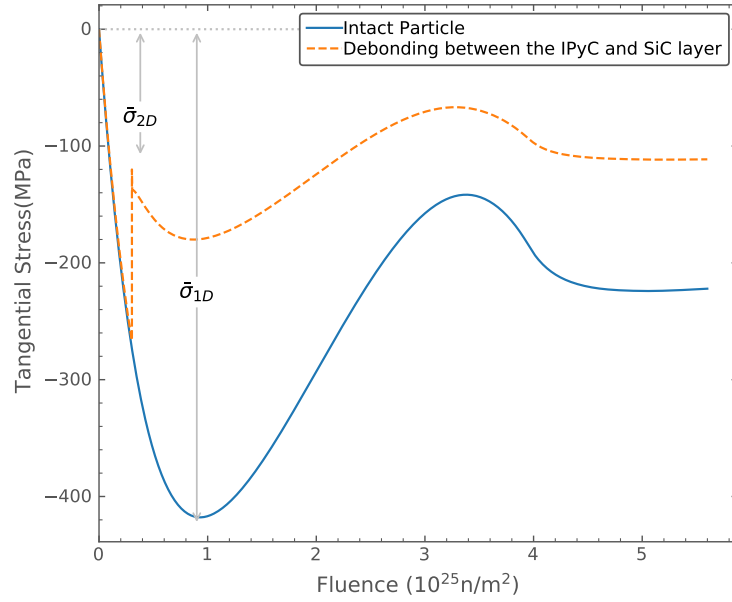


Fig. 29. Time histories of maximum tangential stress in the SiC layer for a 2-D model of a particle with debonding between the IPyC and SiC layer, as compared with a 1-D model of an intact particle. These are used to develop the stress correlation for debonding.

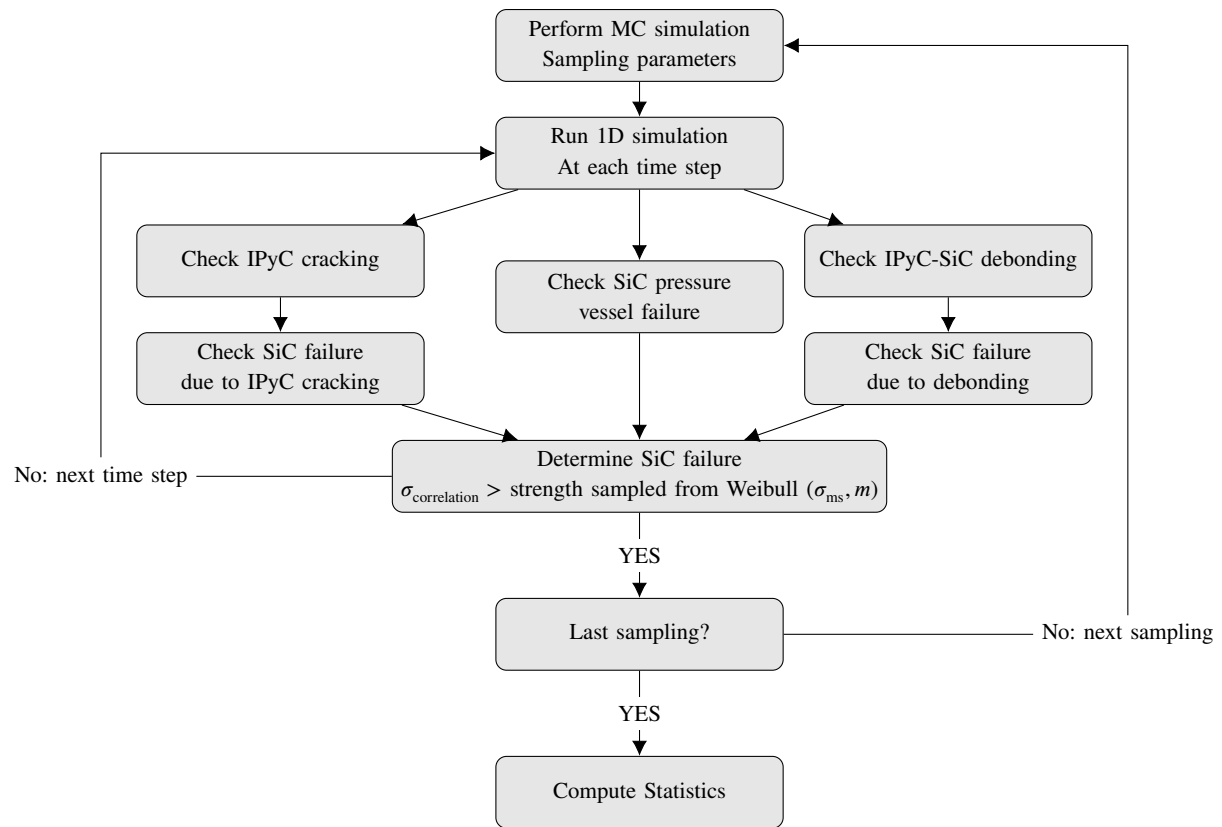


Fig. 30. MC scheme employed by Bison for calculating the failure probability of TRISO particles.

IV. EFFICIENT HIGH-FIDELITY TRISO STATISTICAL FAILURE ANALYSIS

The ability of the TRISO fuel to contain fission products is largely dictated by the quality of the manufacturing process, since most of the fission product release is expected to occur due to coating layer failure in a small number of particles at the defect locations. To account for statistical variation in physical dimensions and material properties from one particle to another, an MC scheme was developed in fiscal year 2020 [4] to compute the failure probability for a statistically sampled batch of particles. One limitation of the MC scheme is that the number of samples must be very large to compute a relatively low failure probability, and the computational resources needed for the task are tremendous. Therefore, it is important to implement a new fast approach in Bison to greatly enhance the efficiency of the failure probability calculation.

A. Failure Modes

Several potential failure mechanisms for TRISO fuel, outlined in the sections below, are considered in the current work. Other failure modes besides those discussed herein are both possible and potentially important, and techniques for considering them are in active development. Several changes made on TRISO material models, as described in Section II, are utilized to increase the accuracy of the simulation results.

1) Pressure vessel failure

Early on during irradiation, PyC shrink, compressing the SiC layer. As irradiation progresses, the creep of the PyC layers tends to relax some of this compressive stress. In addition, the buildup of fission gas pressure tends to put all the coating layers under tension. Since the CO production in a UCO kernel is relatively small, the gas pressure is usually too low to cause the tangential stress in the SiC layer to become tensile. Therefore, pressure vessel failure is unlikely to occur for an intact TRISO UCO kernel at low and intermediate temperatures.

2) Irradiation-induced IPyC failure leading to SiC cracking

During irradiation, shrinkage of the PyC layers causes significant tensile stress in those layers. If the stress exceeds the tensile strength of the material, a radial crack can form in a PyC layer. Such a crack leads to high local tensile stress in the SiC layer adjacent to that cracked PyC layer, potentially causing failure of the SiC layer and, therefore, of the particle. In Figure 31a, a discrete crack in the IPyC layer is represented in the finite element model. The plenum pressure caused by fission gases is applied on crack surfaces. As shown in Figure 31b, the stress in the SiC layer near the crack tip is significantly elevated due to the development of cracking in the IPyC layer. The pressure on crack surfaces makes a larger difference in the SiC stress when there is sufficient buildup of fission gas pressure near the end of the irradiation.

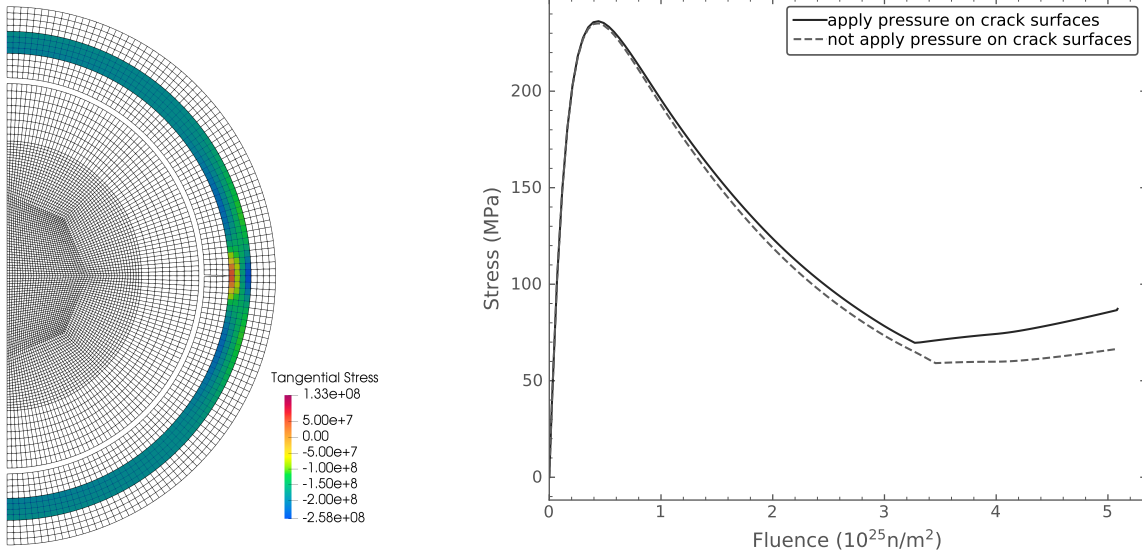
3) Pressure vessel failure of an aspherical particle

A single flat facet on one side of the particle created during fabrication is a common cause of aspherical behavior in particle fuel. During irradiation, the faceted portion of the particle acts as a flat plate that retains the internal gas pressure. If the pressure builds up high enough, this results in a local region of tensile stress in the central portion of the plate, potentially contributing to particle failure. As shown in Figure 32b, the use of local normal vectors predicts a much higher tensile stress at the end of the irradiation. This could have a significant impact on the failure probability calculation.

B. Weibull Failure Theory

A Weibull failure criterion is used to determine vessel failure for the IPyC layer and SiC layer. The maximum stress, σ_c , is compared to a strength sampled from a Weibull distribution featuring mean strength σ_{ms} and Weibull modulus m . Failure occurs when σ_c exceeds the sampled strength. The cumulative distribution function for the Weibull distribution is given as:

$$P = 1 - \exp \left(- \left[\frac{\sigma_c}{\sigma_{ms}} \right]^m \right) \quad (19)$$



(a) Stress contour (Pa) for $T = 1300^\circ\text{C}$ when maximum tangential stress is reached. For clarity, only stresses in the SiC layer are shown.

(b) Time history of peak inner-wall tangential stress in the SiC layer.

Fig. 31. 2-D axisymmetric model of postulated cracking of the IPyC layer, and comparison between applying and not applying pressure on crack surfaces.

The effective mean strength σ_{ms} is given as:

$$\sigma_{ms} = \frac{\sigma_0}{I_n^{1/m}} \quad (20)$$

where σ_0 is the characteristic strength. The integral, I_n , is a normalized integration of the stress distribution using the principle of independent action (PIA) model as follows:

$$I_n = \frac{\int_V (\sigma_1^m + \sigma_2^m + \sigma_3^m) dV}{\sigma_c^m} \quad (21)$$

where σ_c is the maximum value calculated for a principal stress anywhere in the volume and σ_1 , σ_2 , and σ_3 are three principal stresses. Negative principal stresses are not included in this integral because the compressive stresses do not contribute to fracture.

The Weibull modulus (m) and characteristic strength (σ_0) for the SiC are held constant throughout irradiation and are given as:

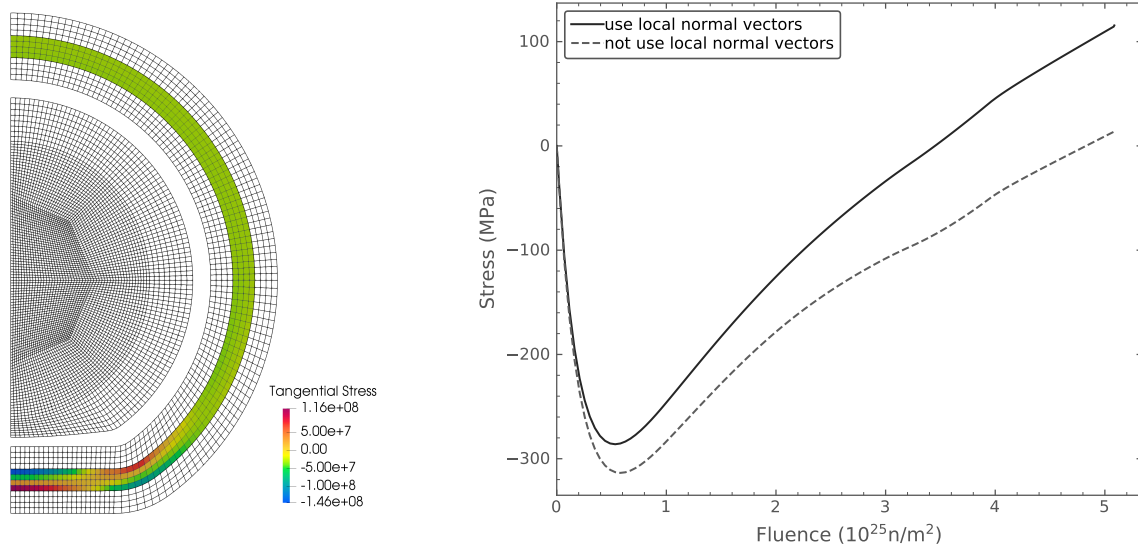
$$m = 6 \quad (22a)$$

and

$$\sigma_0 = 9.64 \times 10^6 \text{ Pa-m}^{3/6} \quad (22b)$$

The Weibull modulus for the PyC is assumed to be 9.5, which corresponds to a density of 1.9 g/cm^3 .

The Weibull characteristic strength of the PyC [9, 10] is a function of anisotropy, and is determined from the



(a) Stress contour (Pa) for $T = 1300^\circ\text{C}$ at end of irradiation, with an aspect ratio of 1.04. For clarity, only stresses in the SiC layer are shown.

(b) Time history of stress in the faceted portion of the SiC layer. Results obtained with and without using the local normal vectors are shown for comparison.

Fig. 32. 2-D axisymmetric model of an aspherical particle, and time-dependent results for that model.

following equation for room temperature:

$$\sigma_0 = 10^6 (154.46X^2 - 141.1X) \quad (23)$$

where X is a fitting parameter with a default value of 1.02. The characteristic strength has units of $\text{Pa}\cdot\text{m}^{3/9.5}$ when the Weibull modulus is 9.5.

To account for other temperatures and non-zero fluence, Equation 23 is multiplied by the following factor:

$$\text{factor} = [(1 + 0.23\phi)(1 + 0.00015T)]^{1/2} \quad (24)$$

where: ϕ = the fast neutron fluence (10^{25} n/m^2 , $E > 0.18 \text{ MeV}$)
 T = the temperature ($^\circ\text{C}$).

C. Higher Order Stress Concentrations

For computational efficiency, it is helpful if each sample is evaluated using a 1-D model. However, stress concentrations due to the presence of phenomena such as cracking must be characterized using a higher dimensional model. To account for these multi-dimensional phenomena within a 1-D TRISO model, a high-dimensional failure simulation is performed to obtain the mean effective strength and stress correlation function, based on a multi-dimensional stress distribution. Those values are used in the 1-D model to make adjustments to the stress in failure determination.

Bison considers a statistical variation of the IPyC, SiC, and OPyC layer thickness because they strongly affect particle failure. To obtain each correlation function $h(\Delta v)$, we typically sample seven points where $\Delta v = -3s, -2s, -s, 0, s, 1s, 2s$, and $3s$, and s is the standard deviation of the thickness. At the midpoint, $h(\Delta v)$ has a value of 1

because $\Delta v = 0$. At other data points, we perform both multi- and one-dimension analysis to determine the value of the correlation function. A polynomial curve fit is finally performed on the data points to generate a quadratic $h(\Delta v)$ function. The correlation functions for the IPyC cracking and aspherical particle are outlined below.

1) Stress correlation for IPyC cracking

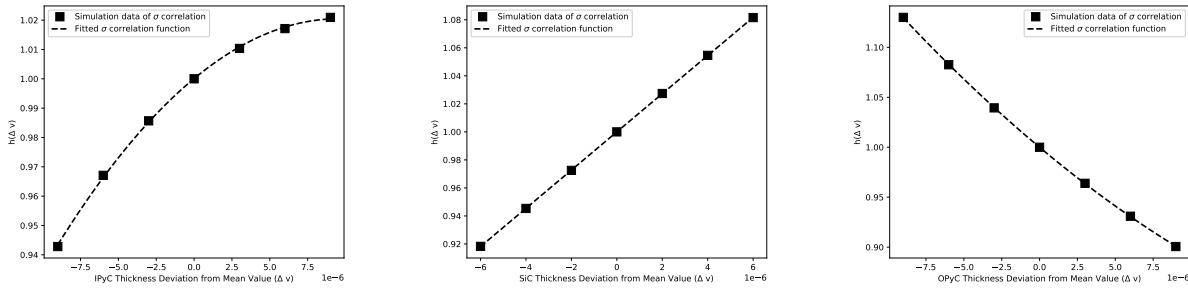
The maximum SiC stress in a cracked particle is approximated as:

$$\sigma_{\text{ipyc-cracking}} = \frac{\bar{\sigma}_{2-D}}{\bar{\sigma}_{1-D}} \sigma_{1-D}(v_{\text{IPyC}}, v_{\text{SiC}}, v_{\text{OPyC}}) h_{\text{IPyC}}(\Delta v_{\text{IPyC}}) h_{\text{SiC}}(\Delta v_{\text{SiC}}) h_{\text{OPyC}}(\Delta v_{\text{OPyC}}) \quad (25)$$

where: $\bar{\sigma}_{2-D}$ = the max. stress calculated in 2-D analyses at the mean values for a specified batch of particles

$\bar{\sigma}_{1-D}$ = the max. stress calculated in 1-D analyses at the mean values for a specified batch of particles.

Upon varying statistical parameters, the maximum stress in the SiC layer is determined from the 1-D finite element solution for σ_{1-D} and the correlation functions. An example stress correlation function for IPyC cracking is shown in Figure 33. The mean strength of the 2-D model, as evaluated at the maximum tangential stress state, will be used for 1-D analysis.



(a) Stress correlation function of IPyC layer thickness for IPyC cracking.

(b) Stress correlation function of SiC layer thickness for IPyC cracking.

(c) Stress correlation function of OPyC layer thickness for IPyC cracking.

Fig. 33. Example of stress correlation functions for IPyC cracking.

2) Stress correlation for an aspherical particle

The tangential stress histories for representative faceted and spherical fuel particles are shown in Figure 34. In evaluating the effect of asphericity, a second term is added to correctly estimate the maximum stress, σ_c , for an aspherical particle:

$$\begin{aligned} \sigma_{\text{aspherical-particle}} = & \frac{\bar{\sigma}_{2-D}}{\bar{\sigma}_{1-D}} \sigma_{1-D-\min}(v_{\text{IPyC}}, v_{\text{SiC}}, v_{\text{OPyC}}) h_{\text{IPyC}}(\Delta v_{\text{IPyC}}) h_{\text{SiC}}(\Delta v_{\text{SiC}}) h_{\text{OPyC}}(\Delta v_{\text{OPyC}}) \\ & + \frac{\Delta \bar{\sigma}_{2-D}}{\Delta \bar{\sigma}_{1-D}} \Delta \sigma_{1-D}(v_{\text{IPyC}}, v_{\text{SiC}}, v_{\text{OPyC}}) h_{\text{IPyC}-\Delta}(\Delta v_{\text{IPyC}}) h_{\text{SiC}-\Delta}(\Delta v_{\text{SiC}}) h_{\text{OPyC}-\Delta}(\Delta v_{\text{OPyC}}) \end{aligned} \quad (26)$$

where $\Delta \bar{\sigma}_{2-D}$, $\Delta \bar{\sigma}_{1-D}$, and $\Delta \sigma_{1-D-\min}$ are changes in the stresses $\bar{\sigma}_{2-D}$, $\bar{\sigma}_{1-D}$, and $\sigma_{1-D-\min}$, respectively, going from the minimum to the end of irradiation. If a second extremum (or maximum) occurs before the end of irradiation, $\Delta \bar{\sigma}_{2-D}$, $\Delta \bar{\sigma}_{1-D}$, and $\Delta \sigma_{1-D}$ are taken as changes in these stresses, going from minimum to maximum. The additional term is needed because pressure vessel failure of aspherical particles typically occurs after the first minimum stress is reached, when shrinkage effects from the PyC are decreasing and the inner pressure is continuing to accumulate. An example stress correlation function for aspherical particles is shown in Figure 34. The mean effective strength of the 2-D model evaluated at the end of irradiation will be used in 1-D analysis.

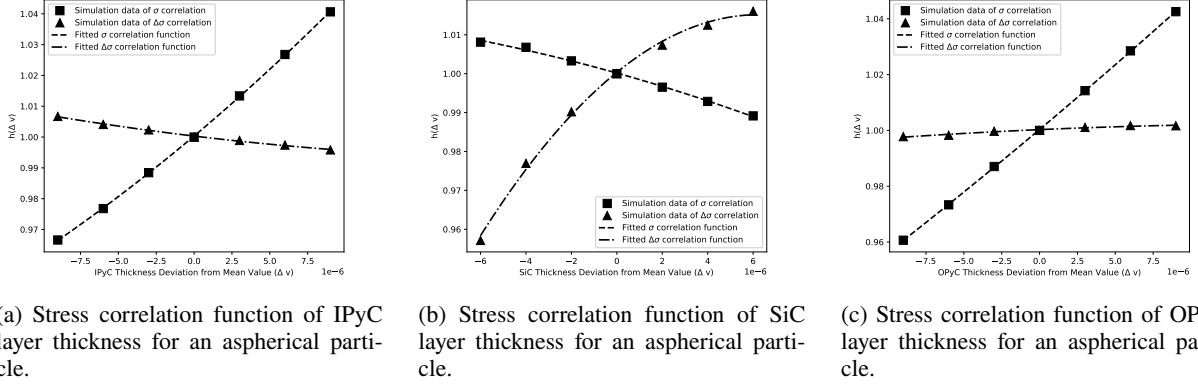


Fig. 34. Example of stress correlation functions for an aspherical particle.

D. Direct Integration Scheme

1) Integration of failure probability function

In an integration approach, the failure probability (Equation 19) for a particle batch will be formulated in terms of an integral. The integral will involve Gaussian statistical distributions for particle design parameters. The failure probability integral is given as:

$$P = \frac{1}{\sqrt{2\pi}^n D_i D_j \dots} \int_{-\infty}^{+\infty} \exp\left(\frac{-[v_i - \mu_i]^2}{2D_i^2}\right) \int_{-\infty}^{+\infty} \exp\left(\frac{-[v_j - \mu_j]^2}{2D_j^2}\right) \dots \left\{ 1 - \exp\left(-\left[\frac{\sigma_c(v_i, v_j, \dots)}{\sigma_{ms}}\right]^m\right) \right\} \quad (27)$$

Numerically evaluating the integration requires an appropriate quadrature rule. A quadrature rule for the normal probability density function (PDF) $\phi(x)$ is a set of N_q points x_q and weights w_q for which the integral can be estimated:

$$\int_{-\infty}^{+\infty} f(x)\phi(x)dx \approx Q(f) = \sum_{q=1}^{N_q} w_q \cdot f(x_q) \quad (28)$$

A quadrature rule with precision k will exactly integrate all polynomials of degree k or less. A Gauss-Hermite quadrature rule for the normal PDF will achieve a precision of $2N_q - 1$. In general, a multi-dimensional quadrature grid is a combination of 1-D quadrature rules. For example, a tensor grid can be described as:

$$\mathcal{A}(D, N_q) = Q_1^{N_q} \otimes \dots \otimes Q_D^{N_q} \quad (29)$$

where D is the number of dimensions and Q_d^j is the one-dimensional quadrature set for dimension d with j points. Note that the number of points used by a tensor grid rule involves raising the number of points in the 1-D rule to the power of the dimensions. To overcome this limitation, a sparse grid method is proposed in order to provide accurate results at a much cheaper cost. The idea behind the efficiency of sparse grids is that, instead of taking the Cartesian product of full order quadrature rules, they use a combination of lower order quadrature rules to complete the monomial space. The sparse grid of a Gauss-Hermite quadrature can significantly reduce the number of points in a high-dimensional space. The sparse grid is described as:

$$A(D, N_q) = \sum_{N_q - D \leq |i| \leq N_q - 1} (-1)^{N_q + D - |i| - 1} \binom{N_q + D - 1}{N_q + D - |i| - 1} (Q_1^{i_1} \otimes \cdots \otimes Q_D^{i_D}) \quad (30)$$

where $|i| = \sum_{d=1}^D i_d$. For more details on sparse grids, please refer to [19].

2) MOOSE Stochastic Tools module

Bison is built on the open-source MOOSE framework [20]. In addition to providing a computational framework for solving partial differential equations, MOOSE also supports stochastic analysis for MOOSE-based applications, including Bison, through its Stochastic Tools module. In previous work [4], the Stochastic Tools module was utilized to perform MC sampling. Because it uses MOOSE's built-in MultiApps system for memory-based data transfer and management of parallel computing resources, it is extremely efficient and scalable. In addition to MC simulation, the Stochastic Tools module can train and evaluate surrogate models using algorithms such as polynomial chaos, proper orthogonal decomposition (POD) reduced basis, and Gaussian processes. This work utilizes the quadrature-based sampling for normal distributions in order to integrate the failure probability function.

To verify implementation of the quadrature rule in MOOSE, we consider the following 2-D integral:

$$I(f) = \frac{1}{\sqrt{2\pi}} e^{-\frac{x^2}{2}} \int_{-\infty}^{+\infty} \frac{1}{\sqrt{2\pi}} e^{-\frac{y^2}{2}} \int_{-\infty}^{+\infty} \frac{1}{x^2 + y^2 + 1} dx dy \quad (31)$$

MATLAB's function `integral2()` gives the (presumably) superior estimate of 0.4614554163 for the above integral. The integration values using MOOSE's tensor grid and sparse grid with different orders of the polynomials is shown in Figure 35. Both the tensor grid and sparse grid schemes converge to MATLAB's solution as the orders increase, though the convergence rate is faster for the tensor grid scheme. For $N_q = 5$, the tensor grid and sparse grid require 36 and 55 quadrature points, and their locations are plotted in Figure 36a and Figure 36b, respectively. The number of quadrature points for different numbers of orders and dimensions for the tensor grid and sparse grid are provided in Table II. In statistical failure analysis of TRISO particles, there are typically 5–10 statistically varying parameters for which the sparse grid scheme can significantly reduce the number of quadrature points.

TABLE II. Number of quadrature points for tensor grid.

N_q	Grid	D=3	D=6	D=9
3	Full	64	4,096	262,144
	Sparse	28	91	190
5	Full	216	46,656	10,077,696
	Sparse	203	1,820	7,315
7	Full	512	252,144	134,217,728
	Sparse	840	18,563	134,596

3) Methodology

A set of statistically varying parameters from the distributions of as-fabricated fuel characteristics (e.g., dimensions and densities) is considered in the integral of Equation 27. The failure probability of IPyC cracking ($P_{\text{IPyC-cracking}}$), SiC failure due to IPyC cracking ($P_{\text{SiC-IPyC-cracking}}$), and pressure vessel failure of aspherical particles ($P_{\text{SiC-PVF}}$) is calculated using sparse grid integration. The overall SiC failure is given as:

$$P_{\text{SiC-overall}} = P_{\text{IPyC-cracking}} \times P_{\text{SiC-IPyC-cracking}} + (1 - P_{\text{IPyC-cracking}}) \times P_{\text{SiC-PVF}} \quad (32)$$

As depicted in Figure 37 and Figure 38, two computation modes were developed to calculate failure probabilities depending on whether the 1-D or 2-D TRISO model is used for each sample. In the first mode, Bison runs the

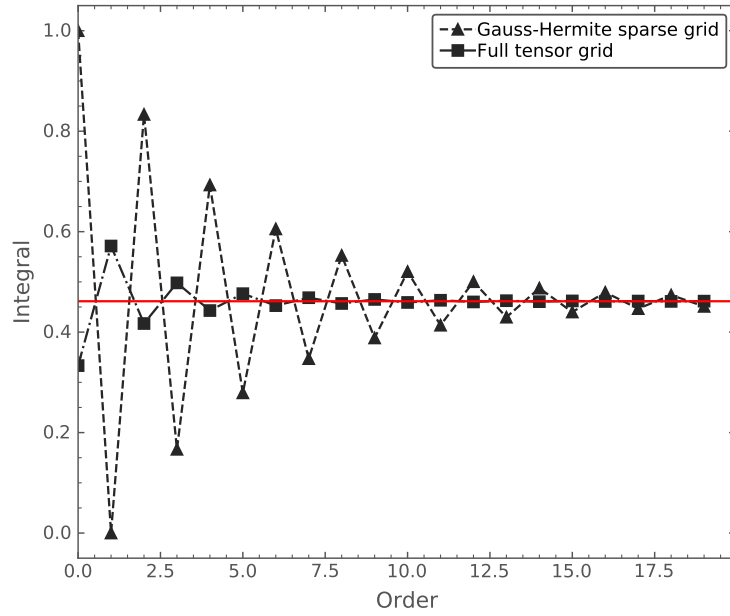


Fig. 35. Integration values using MOOSE's sparse grid with different orders of the polynomials.

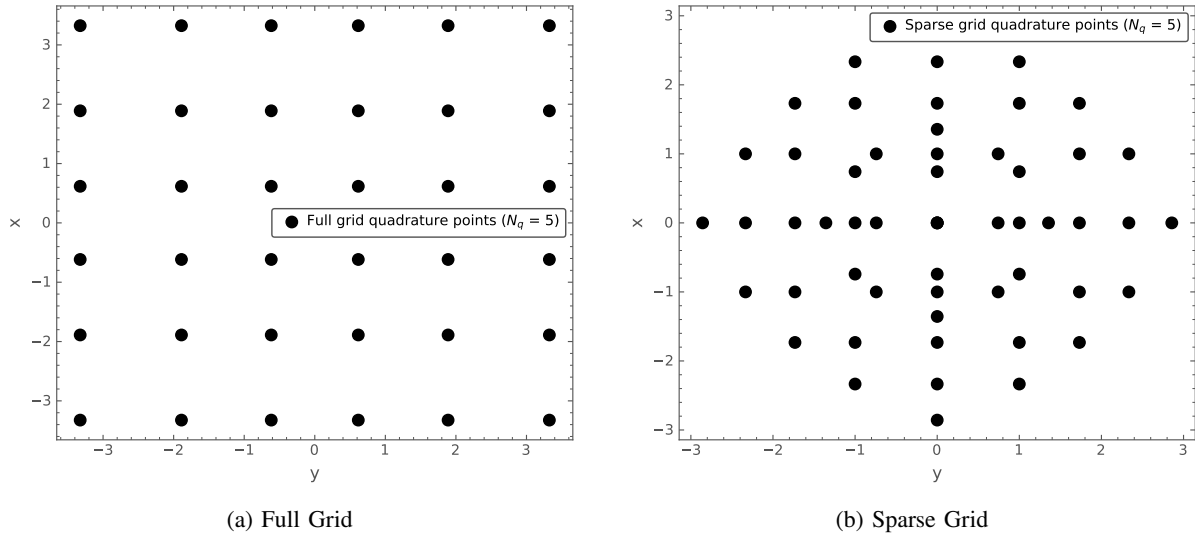


Fig. 36. Quadrature point location.

1-D model of a TRISO particle. For particles with localized flaws (i.e., aspherical particles and particles with cracked IPyC), an adjustment of the maximum stress and effective mean strength will be used, as described in Sections IV-C1 and IV-C2. In the second mode, Bison runs the 2-D model of a TRISO particle. A 2-D aspherical or spherical model will be used to determine the IPyC cracking failure probability and the PVF of the SiC layer, while a 2-D cracked IPyC model will be used to determine SiC layer failure due to IPyC cracking. Although the 1-D

mode requires prior calculation of stress correlation factors and effective mean strength, its computation is much faster. On the other hand, the 2-D mode yields higher accuracy because it directly calculates failure probabilities for high-dimensional failure modes and does not require the use of any stress adjustment. The computation cost of the 2-D mode exceeds that of the 1-D mode, yet remains affordable due to the efficiency of the sparse grid scheme.

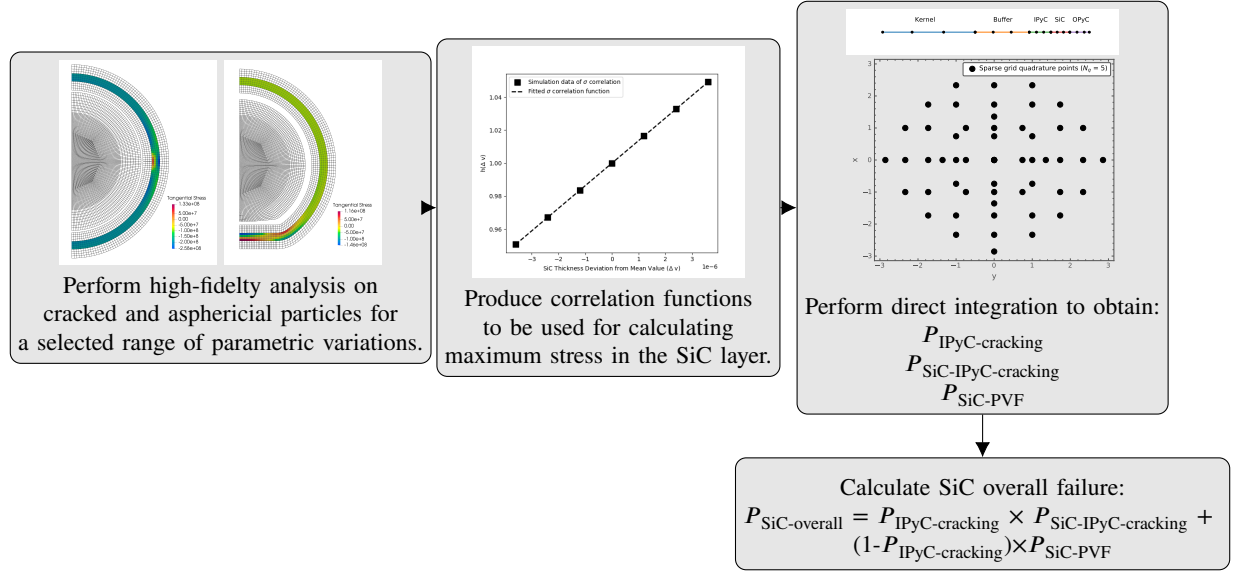


Fig. 37. Calculate the failure probability of TRISO particles in Bison: direct integration scheme using 1-D simulation with correlation functions.

E. Benchmark Problems

To demonstrate Bison's new capability for performing particle failure analysis on particle populations, benchmark testing was performed on a TRISO UCO fuel particle under representative irradiation conditions. These conditions are summarized in Table III. Temperatures of 700, 1000, and 1300°C were chosen so as to fall within the validity range of the material properties. The fuel parameters and their statistical distributions, which are indicated in the last column of Table IV, are based on the AGR-5/6/7 fuel specification.

TABLE III. Irradiation conditions for benchmark problems.

	Conditions		
	1	2	3
Effective full power days (EFPD)	500	500	500
Burnup (%FIMA)	13.5	13.5	13.5
Fast fluence ($\times 10^{25}$ n/m ² , $E > 0.18$ MeV)	5.0	5.0	5.0
Irradiation temperature (°C)	700	1000	1300

The stress correlation functions and effective mean strength are pre-computed for each condition, and their values are listed in Table V and Table VI. The IPyC layer cracking using both MC and direct integration schemes are provided in Table VII. The number of samples for MC simulation is taken as $2000/P_{\text{IPyC-cracking}}$. The results of MC and direct integration show reasonable agreement. For the direct integration scheme, different orders of N_q are

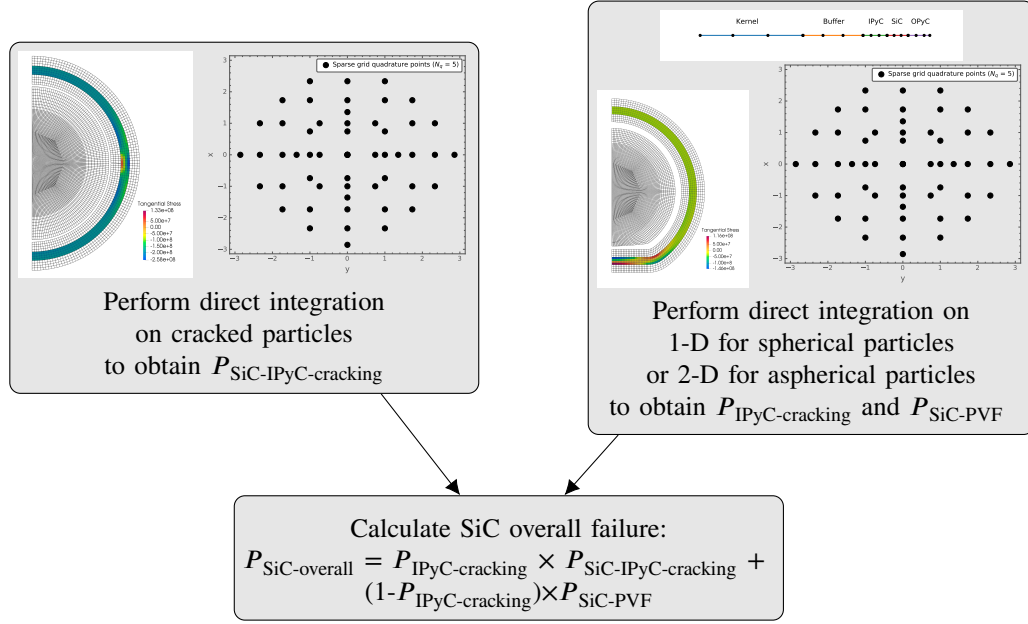


Fig. 38. Calculate the failure probability of TRISO particles in Bison: direct integration scheme using 2-D simulation.

TABLE IV. Fuel parameters in benchmark problems.

Category	Parameter	Nominal values ± Standard Deviation	Statistical Variation
Fuel characteristics	^{235}U enrichment (wt%)	15.5	
	Carbon/uranium (atomic ratio)	0.4	
	Oxygen/uranium (atomic ratio)	1.5	
Particle geometry	Kernel diameter (μm)	425 ± 10	✓
	Buffer thickness (μm)	100 ± 10	✓
	IPyC/OPyC thickness (μm)	40 ± 3	✓
	SiC thickness (μm)	35 ± 2	✓
	Particle asphericity (SiC aspect ratio)	1.04	✓
Fuel properties	Kernel density (g/cm^3)	11.0	
	Kernel theoretical density (g/cm^3)	11.4	
	Buffer density (g/cm^3)	1.05	
	Buffer theoretical density (g/cm^3)	2.25	
	IPyC density (g/cm^3)	1.90 ± 0.02	✓
	OPyC density (g/cm^3)	1.90 ± 0.02	✓
	IPyC/OPyC BAF	1.05 ± 0.005	✓

compared. Increasing the order could improve the accuracy, but the results do not show significant change from $N_q = 5$ to 7. To maintain a good balance between computational cost and accuracy, $N_q = 5$ will be used for our later studies in this report. It is worth mentioning that the 1-D direct integration mode can be at least a hundred

times faster than the MC scheme.

TABLE V. Stress correlation factors and effective mean strength for benchmark problems.

Conditions	Intact	IPyC cracking	Asphericity			
	σ_{ms} (MPa)	σ_{ms} (MPa)	$\frac{\bar{\sigma}_{2-D}}{\bar{\sigma}_{1-D}}$	σ_{ms} (MPa)	$\frac{\bar{\sigma}_{2-D}}{\bar{\sigma}_{1-D}}$	$\frac{\Delta\bar{\sigma}_{2-D}}{\Delta\bar{\sigma}_{1-D}}$
1	711	1406	-1.26	1303	1.54	1.49
2	718	1405	-1.28	1259	1.59	1.78
3	717	1405	-1.29	1405	1.57	2.58

TABLE VI. Quadractic stress correlation functions for benchmark problems.

Conditions	Type	h_{IPyC} function	h_{SiC} function	h_{OPyC} function
1	IPyC cracking (σ)	$1.0 + 4.89 \times 10^3 v - 2.28 \times 10^8 v^2$	$1.0 + 1.36 \times 10^4 v - 6.27 \times 10^6 v^2$	$1.0 - 1.27 \times 10^4 v + 1.84 \times 10^8 v^2$
	Asphericity (σ)	$1.0 + 3.09 \times 10^3 v + 3.16 \times 10^7 v^2$	$1.0 + 6.70 \times 10^2 v - 1.19 \times 10^8 v^2$	$1.0 + 2.89 \times 10^3 v + 4.68 \times 10^6 v^2$
	Asphericity ($\Delta\sigma$)	$1.0 - 1.52 \times 10^3 v - 9.72 \times 10^6 v^2$	$1.0 + 8.69 \times 10^3 v - 5.46 \times 10^8 v^2$	$1.0 + 4.58 \times 10^2 v - 2.13 \times 10^7 v^2$
2	IPyC cracking (σ)	$1.0 + 4.26 \times 10^3 v - 2.30 \times 10^8 v^2$	$1.0 + 1.36 \times 10^4 v - 1.31 \times 10^7 v^2$	$1.0 - 1.27 \times 10^4 v + 1.87 \times 10^8 v^2$
	Asphericity (σ)	$1.0 + 3.86 \times 10^3 v + 3.05 \times 10^7 v^2$	$1.0 - 7.92 \times 10^2 v - 7.23 \times 10^7 v^2$	$1.0 + 3.47 \times 10^3 v + 7.65 \times 10^6 v^2$
	Asphericity ($\Delta\sigma$)	$1.0 + 2.03 \times 10^2 v + 1.42 \times 10^7 v^2$	$1.0 + 1.28 \times 10^3 v - 2.49 \times 10^8 v^2$	$1.0 + 2.79 \times 10^3 v + 6.24 \times 10^6 v^2$
3	IPyC cracking (σ)	$1.0 + 3.96 \times 10^3 v - 2.35 \times 10^8 v^2$	$1.0 + 1.36 \times 10^4 v - 2.30 \times 10^6 v^2$	$1.0 - 1.25 \times 10^4 v + 1.82 \times 10^8 v^2$
	Asphericity (σ)	$1.0 + 4.17 \times 10^3 v + 3.71 \times 10^7 v^2$	$1.0 - 6.10 \times 10^2 v - 6.79 \times 10^7 v^2$	$1.0 + 3.46 \times 10^3 v + 1.83 \times 10^6 v^2$
	Asphericity ($\Delta\sigma$)	$1.0 - 1.89 \times 10^3 v + 2.31 \times 10^7 v^2$	$1.0 - 6.38 \times 10^3 v + 9.66 \times 10^7 v^2$	$1.0 + 2.66 \times 10^3 v + 2.29 \times 10^7 v^2$

TABLE VII. IPyC cracking probability for benchmark problems.

Conditions	MC	Direct Integration			
		$N_q = 1$	$N_q = 3$	$N_q = 5$	$N_q = 7$
1	9.539×10^{-1}	9.627×10^{-1}	9.493×10^{-1}	9.492×10^{-1}	9.491×10^{-1}
2	7.848×10^{-2}	7.533×10^{-2}	7.660×10^{-2}	7.609×10^{-2}	7.596×10^{-2}
3	1.562×10^{-3}	1.487×10^{-3}	1.550×10^{-3}	1.545×10^{-3}	1.553×10^{-3}

Two direct integration modes are used to compute the probability of IPyC layer cracking and SiC layer failure. The results reported in Table VIII show reasonable agreement in IPyC cracking failure probability and SiC failure probability due to IPyC cracking. The 2-D mode predicts a higher PVF probability, particularly at higher irradiation temperatures. This indicates that the correlation function for aspherical particles is less accurate than the one for particles with cracked IPyC. It is worthwhile to mention that the SiC failure probability of condition 3 is so low

TABLE VIII. Failure probability for benchmark problems using Bison's direct integration scheme.

Conditions	Simulation results with $N_q = 5$			
		IPyC cracking	PVF	Overall SiC
1	1-D	9.492×10^{-1}	0	2.653×10^{-3}
	2-D	9.932×10^{-1}	5.405×10^{-10}	2.783×10^{-3}
2	1-D	7.609×10^{-2}	0	2.374×10^{-5}
	2-D	1.999×10^{-1}	1.295×10^{-8}	6.346×10^{-5}
3	1-D	1.545×10^{-3}	4.056×10^{-8}	5.642×10^{-7}
	2-D	7.574×10^{-3}	3.194×10^{-6}	3.407×10^{-6}

that the number of samples needed for MC simulation is beyond Bison's current practical limit of about 100 million samples. This limitation has been overcome by the direct integration mode, for which the number of samples is greatly reduced.

F. AGR-2 Irradiation As-run Prediction

The AGR-2 experiment was the second irradiation experiment performed under the Department of Energy's AGR program. The objective of AGR-2 was to irradiate both UCO and UO_2 TRISO fuel to obtain normal-operation and accident-condition fuel performance data [21, 22]. The AGR-2 experiment was irradiated for 559.2 effective full-power days. Bison models use volume-averaged compact daily temperatures as boundary conditions at the outer edge of the OPyC layer. Use of daily temperatures can largely reflect the thermal state of the compacts throughout irradiation, thereby accurately predicting fission product diffusion and release. The TRISO UCO and UO_2 particle geometries and material properties are listed in Table IX. The irradiation conditions of all AGR-2 compacts are listed in Table X.

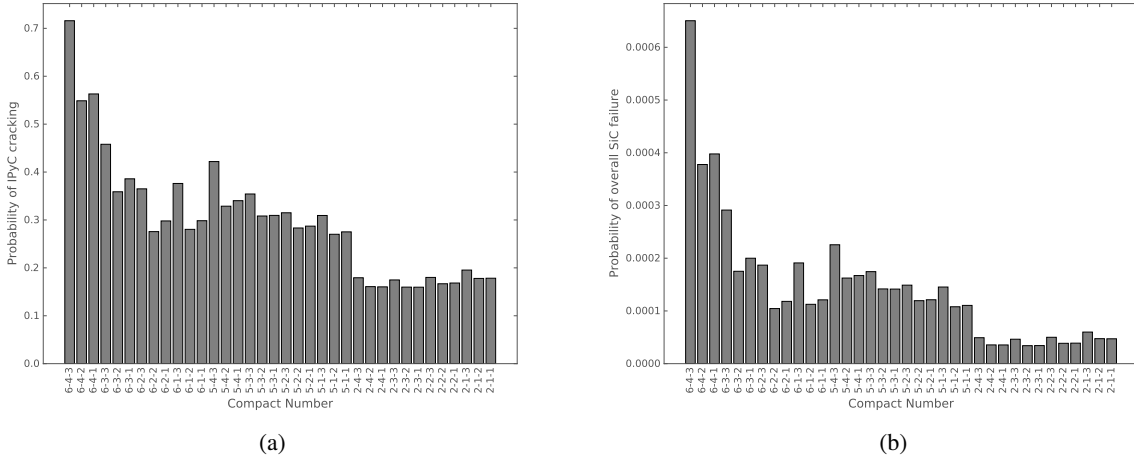
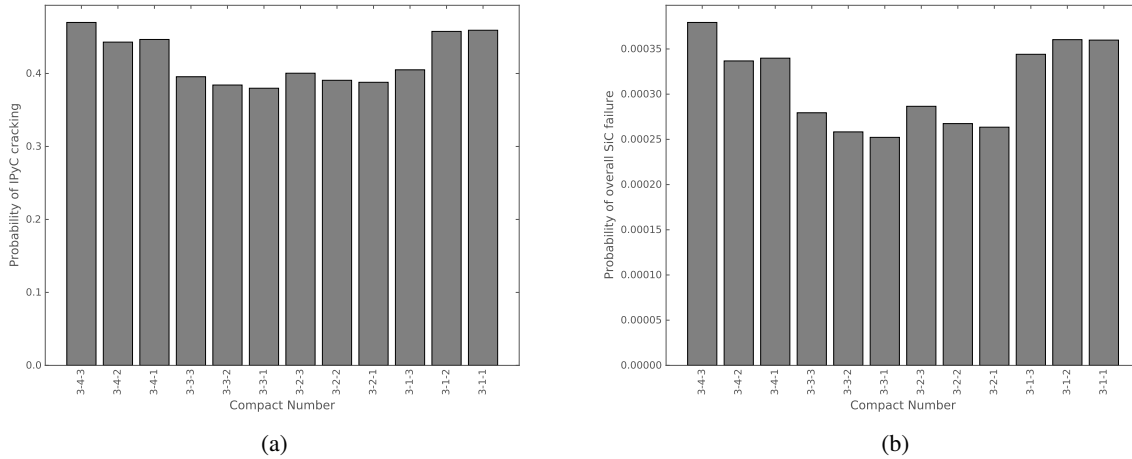


Fig. 39. UCO failure probability: (a) probability of IPyC cracking, and (b) probability of overall SiC failure.

Failure probability calculations are performed here using the 2-D direct integration mode. In this mode, the distribution of the aspect ratio can be also considered. The sampled aspect ratio is used to generate the mesh via

TABLE IX. UCO and UO₂ parameters used in modeling the AGR-2 irradiation.

Category	Parameter	Nominal Values \pm Standard Deviation	
		UCO	UO ₂
Fuel characteristics	²³⁵ U enrichment (wt%)	14.029	9.600
	Carbon/uranium (atomic ratio)	0.392	–
	Oxygen/uranium (atomic ratio)	1.428	2.003
Particle geometry	Kernel diameter (μm)	426.7 ± 8.8	507.7 ± 11.9
	Buffer thickness (μm)	98.9 ± 8.4	97.7 ± 9.9
	IPyC thickness (μm)	40.4 ± 2.5	41.9 ± 3.2
	SiC thickness (μm)	35.2 ± 1.2	41.9 ± 3.2
	OPyC thickness (μm)	43.4 ± 2.9	37.5 ± 1.2
	Particle aspect ratio (SiC)	1.037 ± 0.011	1.034 ± 0.010
Fuel properties	Kernel density (g/cm^3)	10.966 ± 0.033	10.858 ± 0.082
	Kernel theoretical density (g/cm^3)	11.37	10.960
	Buffer density (g/cm^3)	1.05	0.99
	Buffer theoretical density (g/cm^3)	2.25	2.25
	IPyC density (g/cm^3)	1.89 ± 0.0011	1.900 ± 0.05
	OPyC density (g/cm^3)	1.907 ± 0.007	1.884 ± 0.004
	IPyC BAF	1.0465 ± 0.0049	1.0471 ± 0.0036
	OPyC BAF	1.0429 ± 0.0019	1.0365 ± 0.0016

Fig. 40. UO₂ failure probability: (a) probability of IPyC cracking, and (b) probability of overall SiC failure.

Bison's built-in TRISO mesh generator. Table XI summarizes the failure probabilities of IPyC cracking, PVF, and overall SiC failure. The PVF probability is negligible compared to that of SiC failure due to IPyC cracking. The UCO and UO₂ failure probabilities are shown in Figure 39 and Figure 40, respectively. A linear regression is performed on UCO compacts to establish the relationship between the failure probability and irradiation conditions (i.e., temperature, fluence, and burnup). As shown in Figure 41 and Figure 42, the probability of IPyC cracking and

TABLE X. Compacts used in modeling the AGR-2 irradiation.

Compact	Fuel Type	Fluence (10^{25} n/m ²) [E>0.18 MeV]	Burnup (%FIMA)	Avg. Temp. (°C)	Compact	Fuel Type	Fluence (10^{25} n/m ²) [E>0.18 MeV]	Burnup (%FIMA)	Avg. Temp. (°C)
6-4-3	UCO	1.94	7.27	987	3-4-3	UO ₂	3.10	9.33	998
6-4-2	UCO	2.21	9.27	1018	3-4-2	UO ₂	3.50	10.71	1013
6-4-1	UCO	2.20	9.25	1018	3-4-1	UO ₂	3.47	10.65	1013
6-3-3	UCO	2.14	7.47	1060	3-3-3	UO ₂	3.11	9.09	1046
6-3-2	UCO	2.43	9.61	1094	3-3-2	UO ₂	3.53	10.56	1062
6-3-1	UCO	2.42	9.60	1094	3-3-1	UO ₂	3.49	10.49	1062
6-2-3	UCO	2.30	8.23	1095	3-2-3	UO ₂	3.09	9.03	1045
6-2-2	UCO	2.61	10.20	1129	3-2-2	UO ₂	3.51	10.54	1062
6-2-1	UCO	2.60	10.18	1129	3-2-1	UO ₂	3.47	10.45	1061
6-1-3	UCO	2.42	9.10	1069	3-1-3	UO ₂	3.05	9.27	996
6-1-2	UCO	2.73	10.83	1100	3-1-2	UO ₂	3.45	10.69	1012
6-1-1	UCO	2.73	10.79	1100	3-1-1	UO ₂	3.41	10.62	1011
5-4-3	UCO	2.78	10.09	1040	2-4-3	UCO	3.08	11.53	1216
5-4-2	UCO	3.14	12.05	1071	2-4-2	UCO	3.47	13.17	1240
5-4-1	UCO	3.13	12.07	1071	2-4-1	UCO	3.44	13.14	1240
5-3-3	UCO	2.91	10.08	1093	2-3-3	UCO	3.06	11.02	1270
5-3-2	UCO	3.29	12.10	1126	2-3-2	UCO	3.46	12.07	1296
5-3-1	UCO	3.28	12.05	1126	2-3-1	UCO	3.42	12.65	1296
5-2-3	UCO	3.00	10.44	1108	2-2-3	UCO	2.99	10.82	1261
5-2-2	UCO	3.39	12.36	1141	2-2-2	UCO	3.39	12.57	1287
5-2-1	UCO	3.38	12.30	1141	2-2-1	UCO	3.35	12.49	1287
5-1-3	UCO	3.03	11.10	1078	2-1-3	UCO	2.88	10.96	1194
5-1-2	UCO	3.43	12.90	1109	2-1-2	UCO	3.25	12.64	1219
5-1-1	UCO	3.41	12.82	1108	2-1-1	UCO	3.21	12.55	1218

overall SiC failure increases as temperature, fluence, and burnup decrease. The lower temperature causes less creep of the IPyC layer to offset the shrinkage and relieve tensile stress, thus increasing the probability of IPyC cracking, as well as SiC failure due to IPyC cracking. For all compacts, histories of the inner-wall tangential stresses in the SiC of an intact particle, a particle with IPyC cracking, and an aspherical particle are plotted in Figure 43 through Figure 45. Spikes on those curves are mainly caused by fluctuations in daily temperature history.

TABLE XI. Failure probability for AGR-2 compacts.

Compact	IPyC cracking	PVF	Overall SiC	Compact	IPyC cracking	PVF	Overall SiC
6-4-3	7.1592×10^{-1}	1.1509×10^{-8}	6.5044×10^{-4}	3-4-3	4.6992×10^{-1}	1.1448×10^{-8}	3.7933×10^{-4}
6-4-2	5.4877×10^{-1}	1.3124×10^{-8}	3.7774×10^{-4}	3-4-2	4.4298×10^{-1}	1.1135×10^{-8}	3.3676×10^{-4}
6-4-1	5.6305×10^{-1}	1.3422×10^{-8}	3.9778×10^{-4}	3-4-1	4.4662×10^{-1}	1.1187×10^{-8}	3.3982×10^{-4}
6-3-3	4.5798×10^{-1}	1.4561×10^{-8}	2.9132×10^{-4}	3-3-3	3.9553×10^{-1}	1.1346×10^{-8}	2.7942×10^{-4}
6-3-2	3.5883×10^{-1}	1.4066×10^{-8}	1.7520×10^{-4}	3-3-2	3.8417×10^{-1}	1.1008×10^{-8}	2.5826×10^{-4}
6-3-1	3.8588×10^{-1}	1.4387×10^{-8}	1.9998×10^{-4}	3-3-1	3.7978×10^{-1}	1.0983×10^{-8}	2.5222×10^{-4}
6-2-3	3.6494×10^{-1}	1.4667×10^{-8}	1.8687×10^{-4}	3-2-3	4.0035×10^{-1}	1.1202×10^{-8}	2.8657×10^{-4}
6-2-2	2.7567×10^{-1}	1.1343×10^{-8}	1.0450×10^{-4}	3-2-2	3.9065×10^{-1}	1.1011×10^{-8}	2.6744×10^{-4}
6-2-1	2.9795×10^{-1}	1.2846×10^{-8}	1.1813×10^{-4}	3-2-1	3.8792×10^{-1}	1.0997×10^{-8}	2.6348×10^{-4}
6-1-3	3.7619×10^{-1}	1.4286×10^{-8}	1.9105×10^{-4}	3-1-3	4.0501×10^{-1}	1.2732×10^{-8}	3.4410×10^{-4}
6-1-2	2.8038×10^{-1}	1.2311×10^{-8}	1.1257×10^{-4}	3-1-2	4.5765×10^{-1}	1.1119×10^{-8}	3.6029×10^{-4}
6-1-1	2.9842×10^{-1}	1.2440×10^{-8}	1.2103×10^{-4}	3-1-1	4.5924×10^{-1}	1.1181×10^{-8}	3.5980×10^{-4}
5-4-3	4.2191×10^{-1}	1.4100×10^{-8}	2.2551×10^{-4}	2-4-3	1.7933×10^{-1}	9.6448×10^{-9}	4.9222×10^{-5}
5-4-2	3.2875×10^{-1}	1.4426×10^{-8}	1.6237×10^{-4}	2-4-2	1.6080×10^{-1}	7.6879×10^{-9}	3.5564×10^{-5}
5-4-1	3.4023×10^{-1}	1.3955×10^{-8}	1.6710×10^{-4}	2-4-1	1.6031×10^{-1}	7.7381×10^{-9}	3.5491×10^{-5}
5-3-3	3.5421×10^{-1}	1.4292×10^{-8}	1.7454×10^{-4}	2-3-3	1.7477×10^{-1}	9.3469×10^{-9}	4.6364×10^{-5}
5-3-2	3.0824×10^{-1}	1.4027×10^{-8}	1.4174×10^{-4}	2-3-2	1.5981×10^{-1}	7.3440×10^{-9}	3.4118×10^{-5}
5-3-1	3.0951×10^{-1}	1.3969×10^{-8}	1.4145×10^{-4}	2-3-1	1.5966×10^{-1}	7.4163×10^{-9}	3.4295×10^{-5}
5-2-3	3.1498×10^{-1}	1.3842×10^{-8}	1.4890×10^{-4}	2-2-3	1.8004×10^{-1}	9.7045×10^{-9}	5.0034×10^{-5}
5-2-2	2.8324×10^{-1}	1.3447×10^{-8}	1.1945×10^{-4}	2-2-2	1.6680×10^{-1}	8.0354×10^{-9}	3.8616×10^{-5}
5-2-1	2.8710×10^{-1}	1.3421×10^{-8}	1.2121×10^{-4}	2-2-1	1.6834×10^{-1}	7.9559×10^{-9}	3.8916×10^{-5}
5-1-3	3.0936×10^{-1}	1.4135×10^{-8}	1.4535×10^{-4}	2-1-3	1.9539×10^{-1}	1.0612×10^{-8}	5.9914×10^{-5}
5-1-2	2.7011×10^{-1}	1.2928×10^{-8}	1.0793×10^{-4}	2-1-2	1.7795×10^{-1}	9.3062×10^{-9}	4.7405×10^{-5}
5-1-1	2.7513×10^{-1}	1.2922×10^{-8}	1.1050×10^{-4}	2-1-1	1.7838×10^{-1}	9.2066×10^{-9}	4.7167×10^{-5}

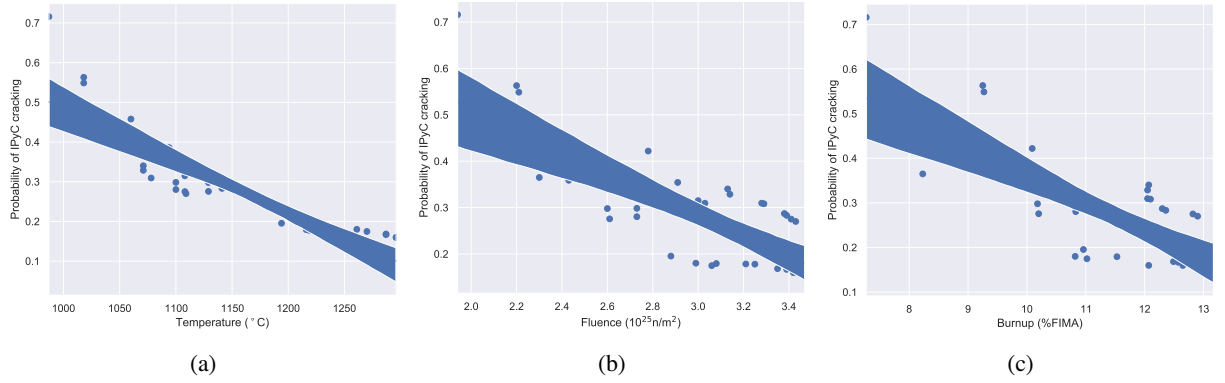


Fig. 41. Linear regression results for UCO compacts: (a) temperature vs. probability of IPyC cracking, (b) fluence vs. probability of IPyC cracking, and (c) burnup vs. probability of IPyC cracking.

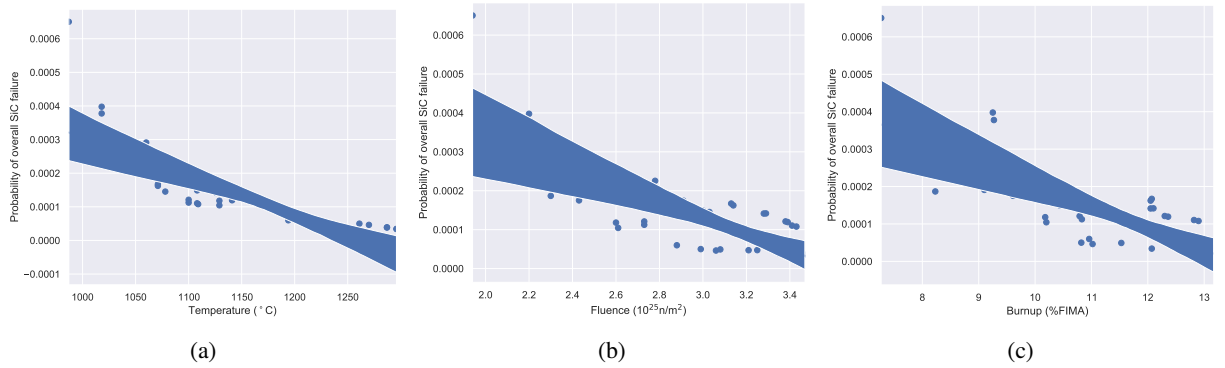


Fig. 42. Linear regression results for UCO compacts: (a) temperature vs. probability of IPyC cracking, (b) fluence vs. probability of IPyC cracking, and (c) burnup vs. probability of overall SiC failure.

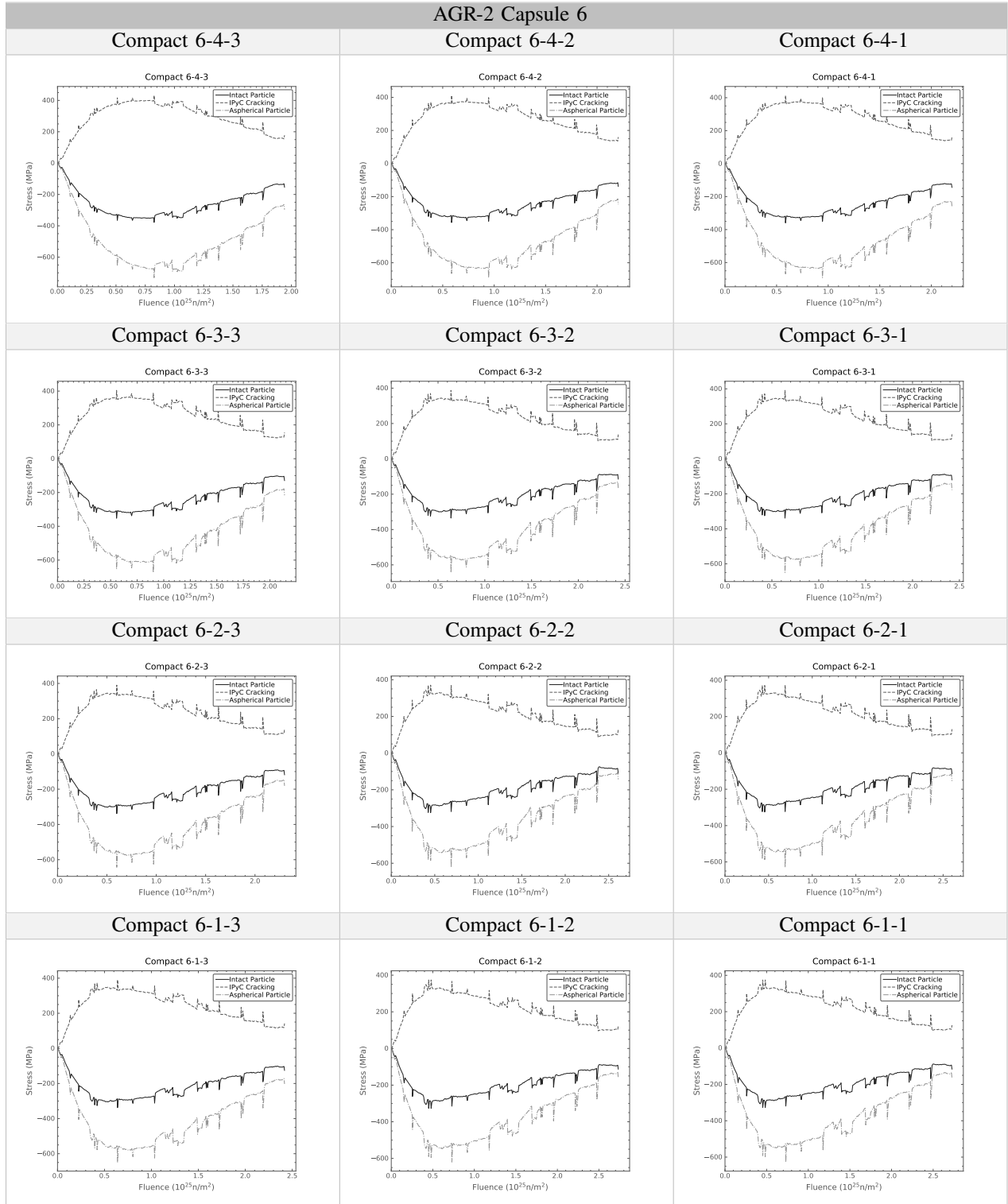


Fig. 43. Inner-wall tangential stress histories in the SiC layer for AGR-2 Capsule 6 compacts.

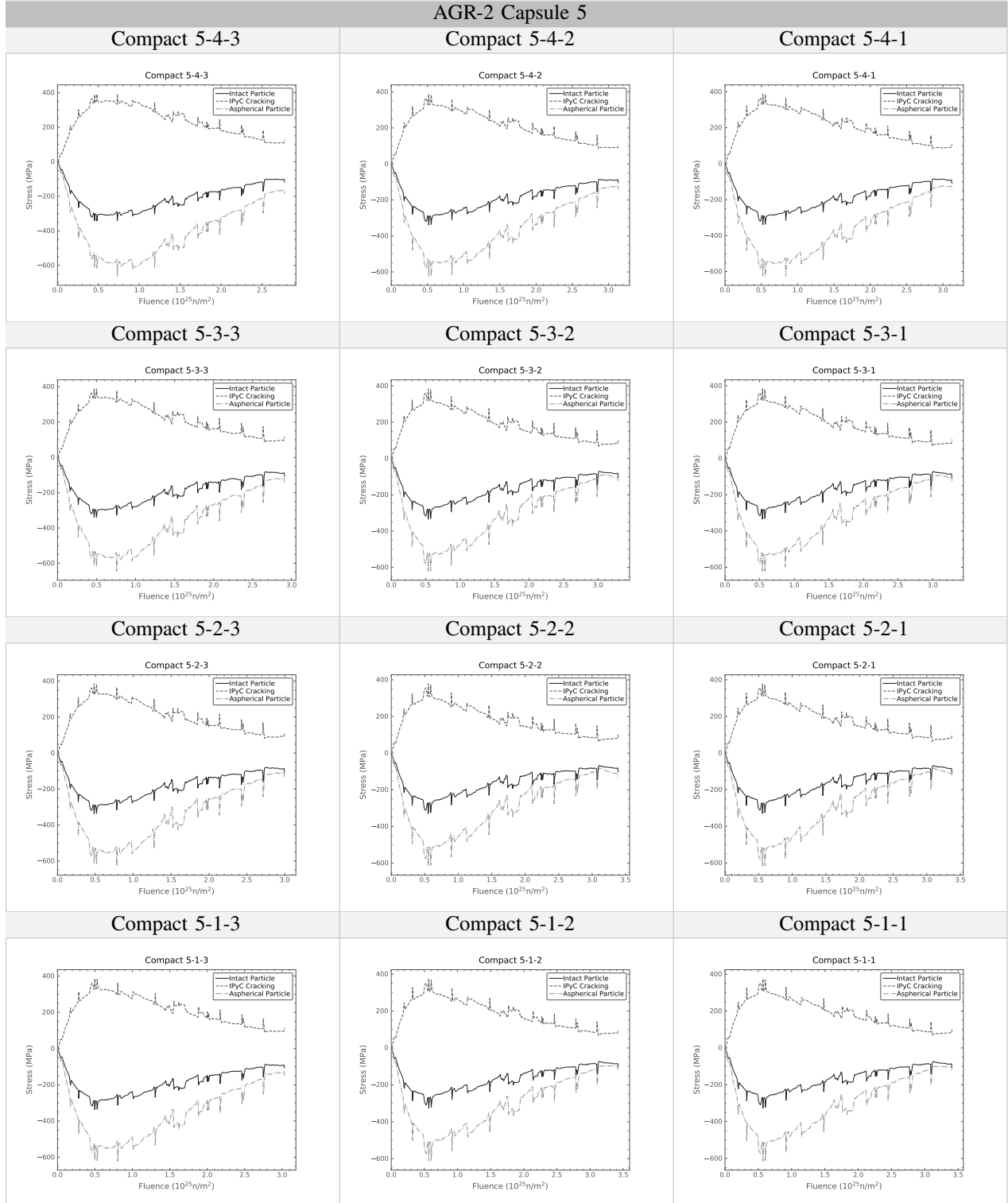


Fig. 44. Inner-wall tangential stress histories in the SiC layer for AGR-2 Capsule 5 compacts.

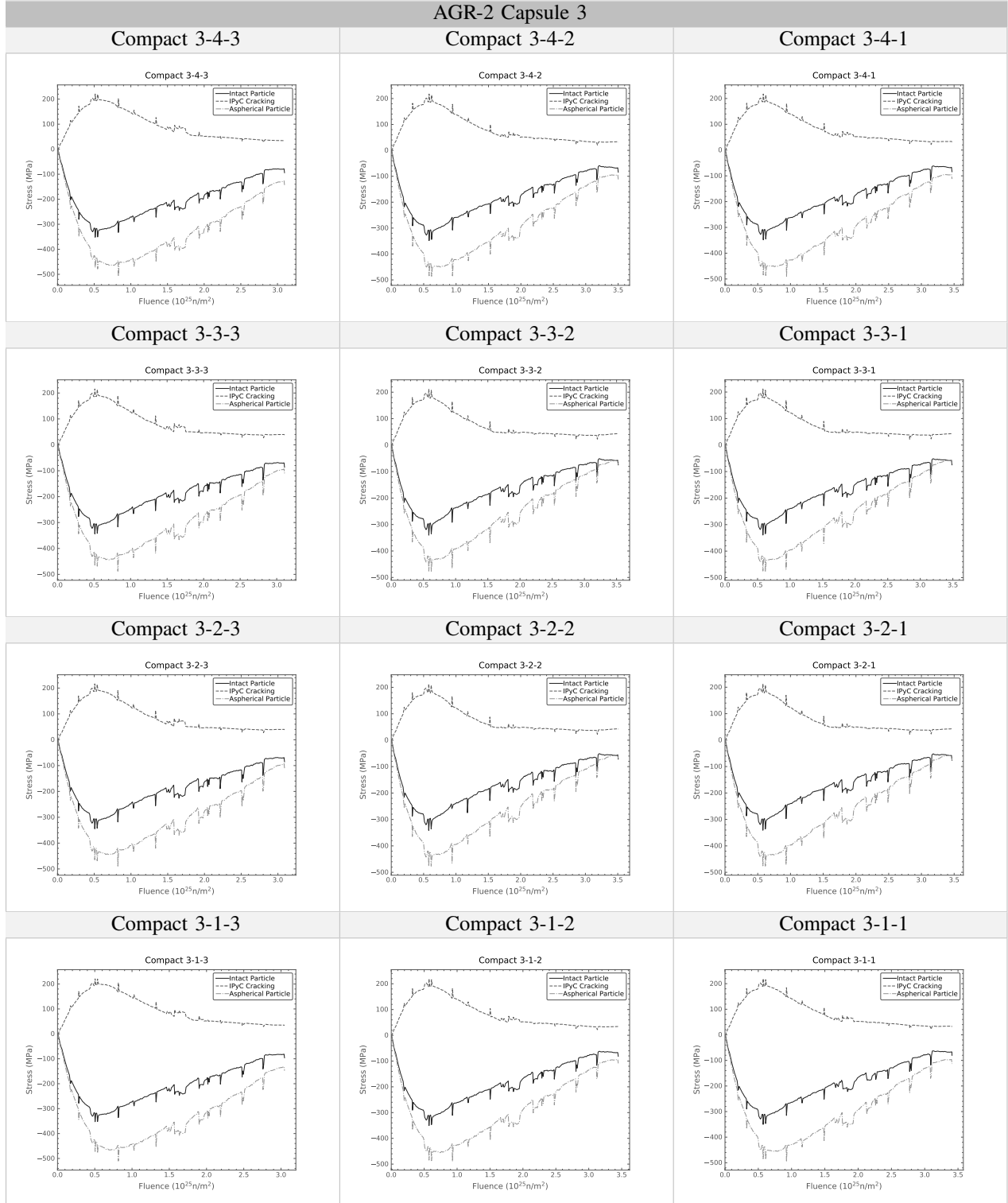


Fig. 45. Inner-wall tangential stress histories in the SiC layer for AGR-2 Capsule 3 compacts.

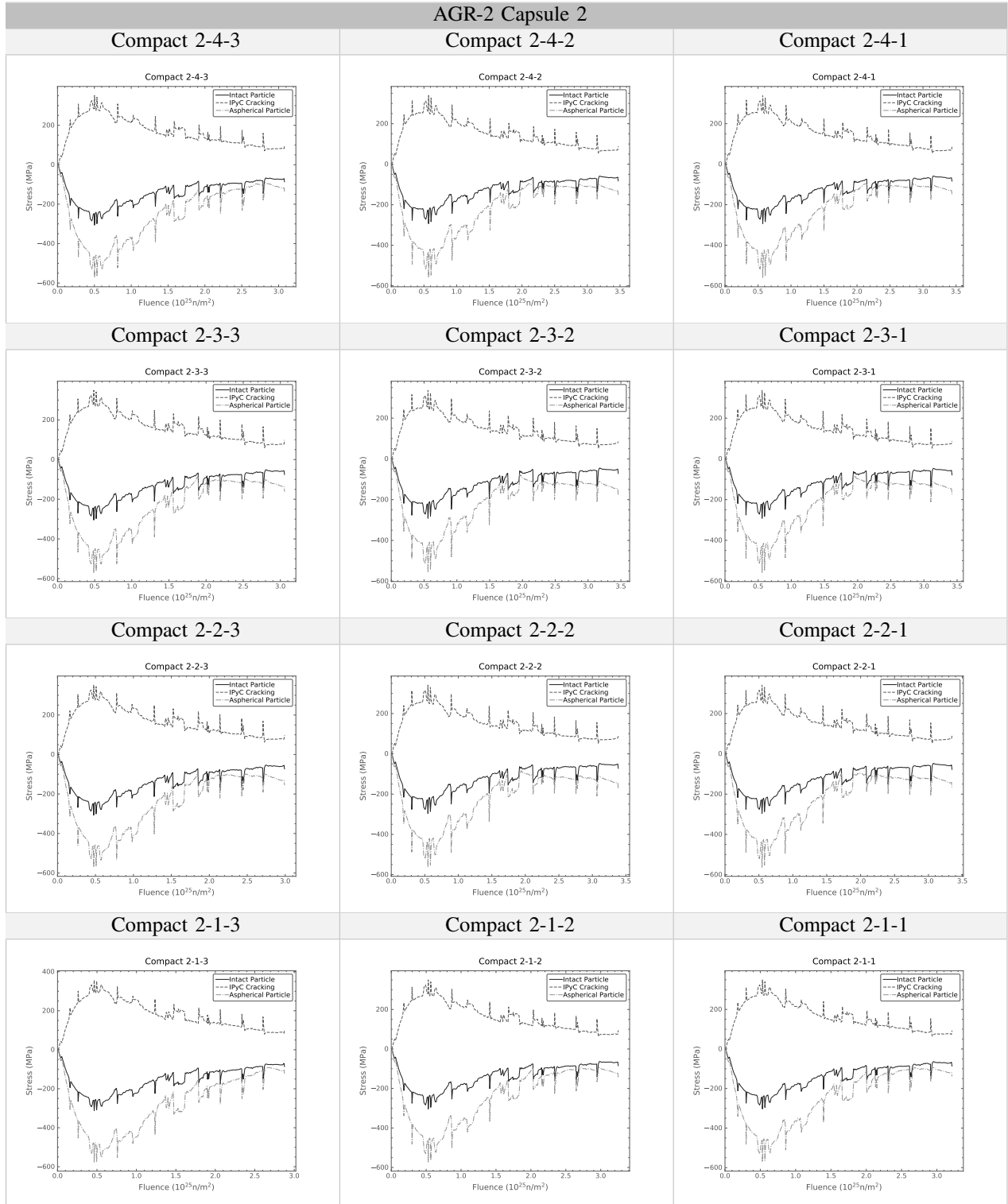


Fig. 46. Inner-wall tangential stress histories in the SiC layer for AGR-2 Capsule 2 compacts.

V. CONCLUSION AND FUTURE WORK

The capabilities of Bison have been significantly expanded to enable it to model the fuel performance of TRISO particles. Recent examples of such development include incorporating anisotropy in the elasticity model of PyC and using the local coordinate system for aspherical particle geometry. The capability of modeling interface debonding in TRISO particles was also developed in Bison. The effect of debonding on the thermo-mechanical behavior of TRISO particles was investigated in several numerical examples. A new capability was developed to calculate failure probability using a sparse grid sampling approach. This new approach can be over a hundred times faster than the MC scheme, particularly when the failure probability is low. It also allows for directly running high-fidelity 2-D models to yield high accuracy. All these capabilities were tested extensively, including on benchmark problems and AGR-2 as-run tests.

Future work will involve developing an anisotropic PyC thermal model in Bison. The robustness of the debonding model needs further improvement. The recently developed Mortar contact capability has yet to be introduced to model the contact between debonded layers. In addition, the debonding failure mode must be incorporated into the direct integration approach, requiring a resolution process to determine a differential particle failure probability for each of the several failure modes.

REFERENCES

- [1] R. L. Williamson et al. “BISON: A flexible code for advanced simulation of the performance of multiple nuclear forms”. In: *Nuclear Technology* 207.7 (2021), pp. 954–980. DOI: 10.1080/00295450.2020.1836940.
- [2] J.D. Hales et al. “Multidimensional multiphysics simulation of TRISO particle fuel”. In: *Journal of Nuclear Materials* 443.1–3 (Nov. 2013), pp. 531–543. DOI: 10.1016/j.jnucmat.2013.07.070.
- [3] J. D. Hales et al. *BISON TRISO Modeling Advancements and Validation to AGR-1 Data*. PEMP Notable Outcome 1.1.C Completion Report INL/EXT-20-59368. Idaho Falls, ID United States: Idaho National Laboratory (INL), Sept. 2020. DOI: 10.2172/1711423. URL: <https://www.osti.gov/biblio/1711423/>.
- [4] W. Jiang et al. “TRISO particle fuel performance and failure analysis with BISON”. In: *Journal of Nuclear Materials* 548 (May 2021), p. 152795. DOI: 10.1016/j.jnucmat.2021.152795.
- [5] J. D. Hales et al. “Modeling fission product diffusion in TRISO fuel particles with BISON”. In: *Journal of Nuclear Materials* 548 (May 2021), 152840:1–16. DOI: 10.1016/j.jnucmat.2021.152840.
- [6] J. D. Hales et al. “Numerical Evaluation of AGR-2 Fission product release (*under journal review*)”. In: (2021).
- [7] A. Toptan et al. “FEA-aided investigation of the effective thermal conductivity in a medium with embedded spheres”. In: *Nuclear Engineering and Design* 381 (Sept. 2021), p. 111355. DOI: 10.1016/j.nucengdes.2021.111355.
- [8] W. Jiang et al. *Fission product transport in TRISO particles and pebbles*. Tech. rep. INL/EXT-21-63549. Idaho Falls, ID United States: Idaho National Laboratory (INL), 2021. DOI: 10.2172/1818294. URL: <https://www.osti.gov/biblio/1818294>.
- [9] G. K. Miller et al. *PARFUME Theory and Model Basis Report*. Tech. rep. INL/EXT-08-14497 (Rev.1). Idaho Falls, ID (United States): Idaho National Laboratory (INL), Sept. 2018. DOI: 10.2172/1471713. URL: <https://www.osti.gov/biblio/1471713-parfume-theory-model-basis-report>.
- [10] F. Ho. *NP-MHTGR: Material Models of Pyrocarbon and Pyrolytic Silicon Carbide*. Tech. rep. CEGA-002820 Rev. 1. CEGA Corporation, July 1993.
- [11] P. A. Demkowicz et al. “Irradiation performance of AGR-1 high temperature reactor fuel”. In: *Nuclear Engineering and Design* 306 (Sept. 2016). 7th International Topical Meeting on High Temperature Reactor Technology (HTR 2014), pp. 2–13. DOI: 10.1016/j.nucengdes.2015.09.011.
- [12] F. J. Rice, J. D. Stempien, and P. A. Demkowicz. “Ceramography of irradiated TRISO fuel from the AGR-2 experiment”. In: *Nuclear Engineering and Design* 329 (2018). The Best of HTR 2016: International Topical Meeting on High Temperature Reactor Technology, pp. 73–81. ISSN: 0029-5493. DOI: 10.1016/j.nucengdes.2017.10.010.
- [13] J. D. Hunn et al. “Detection and analysis of particles with failed SiC in AGR-1 fuel compacts”. In: *Nuclear Engineering and Design* 306 (2016). 7th International Topical Meeting on High Temperature Reactor Technology (HTR 2014), pp. 36–46. DOI: 10.1016/j.nucengdes.2015.12.011.
- [14] A. Rovinelli and M. C. Messner. *Identify the influence of microstructure on mesoscale creep and fatigue damage*. Tech. rep. ANL-20/49. Argonne National Laboratory, Sept. 2020. DOI: 10.2172/1658575. URL: <https://www.osti.gov/biblio/1658575>.
- [15] P. P. Camanho and C. G. Dávila. *Mixed-Mode Decohesion Finite Elements for the Simulation of Delamination in Composite Materials*. Tech. rep. NASA/TM-2002-211737. National Aeronautics and Space Administration (NASA), 2002.
- [16] M.L. Benzeggagh and M. Kenane. “Measurement of mixed-mode delamination fracture toughness of unidirectional glass/epoxy composites with mixed-mode bending apparatus”. In: *Composites Science and Technology* 56.4 (1996), pp. 439–449. DOI: [https://doi.org/10.1016/0266-3538\(96\)00005-X](https://doi.org/10.1016/0266-3538(96)00005-X).
- [17] A. Toptan, D. J. Kropaczek, and M. N. Avramova. “Gap conductance modeling I: Theoretical considerations on the model for single- and multi-component gases”. In: *Nuclear Engineering and Design* 353 (Dec. 2019), 110283:1–7. DOI: 10.1016/j.nucengdes.2019.110283.

- [18] R. B. Bird, W. E. Stewart, and E. N. Lightfoot. *Transport Phenomena*. New York, New York: John Wiley & Sons, Inc., 1960.
- [19] T. Gerstner and M. Griebel. “Numerical integration using sparse grids”. In: *Numerical Algorithms* 18.3 (Jan. 1998), pp. 1572–9265. DOI: 10.1023/A:1019129717644.
- [20] C. J. Permann et al. “MOOSE: Enabling massively parallel multiphysics simulation”. In: *SoftwareX* 11 (2020), p. 100430. DOI: 10.1016/j.softx.2020.100430.
- [21] B.P. Collin. *AGR-2 Irradiation Test Plan*. Tech. rep. PLN-3798 (Rev.2). Idaho National Laboratory (INL), Feb. 2018.
- [22] B.P. Collin. *AGR-2 Irradiation Test Final As-Run Report*. Tech. rep. INL/EXT-14-32277 (Rev.4). Idaho National Laboratory (INL), Feb. 2018. DOI: 10.2172/1514716. URL: <https://www.osti.gov/biblio/1514716-agr-irradiation-test-final-run-report-rev>.